ACS OMEGA

Open Access



http://pubs.acs.org/journal/acsodf

Article

# Plain-Woven Areca Sheath Fiber-Reinforced Epoxy Composites: The Influence of the Fiber Fraction on Physical and Mechanical Features and Responses of the Tribo System and Machine Learning Modeling

Suresh Poyil Subramanyam, Dilip Kumar Kotikula, Basavaraju Bennehalli, Atul Babbar, Sagr Alamri, Alaauldeen A. Duhduh, Ali A. Rajhi, Raman Kumar,* and Ketan Kotecha*

Cite This: *ACS Omega* 2024, 9, 8019−8036

Read Online

ACCESS | Metrics & More | Article Recommendations

**ABSTRACT:** Recent studies focus on enhancing the mechanical features of natural fiber composites to replace synthetic fibers that are highly useful in the building, automotive, and packing industries. The novelty of the work is that the woven areca sheath fiber (ASF) with different fiber fraction epoxy composites has been fabricated and tested for its tribological responses on three-body abrasion wear testing machines along with its mechanical features. The impact of the fiber fraction on various features is examined. The study also revolves around the development and validation of a machine learning predictive model using the random forest (RF) algorithm, aimed at forecasting two critical performance parameters: the specific wear rate (SWR) and the coefficient of friction (COF). The void fraction is observed to vary between 0.261 and 3.8% as the fiber fraction is incremented. The hardness of the mat rises progressively from 40.23 to 84.26 HRB. A fair ascent in the tensile strength and its modulus is also observed. Even though a short descent in flexural strength and its modulus is seen for 0 to 12 wt % composite specimens, they incrementally raised to the finest values of 52.84 and 2860 MPa, respectively, pertinent to the 48 wt % fiber-loaded specimen. A progressive rise in the ILSS and impact strength is perceptible. The wear behavior of the specimens is reported. The worn surface morphology is studied to understand the interface of the ASF with the epoxy matrix. The RF model exhibited outstanding predictive prowess, as evidenced by high *R*-squared values coupled with low mean-square error and mean absolute error metrics. Rigorous statistical validation employing paired *t* tests confirmed the model's suitability, revealing no significant disparities between predicted and actual values for both the SWR and COF.

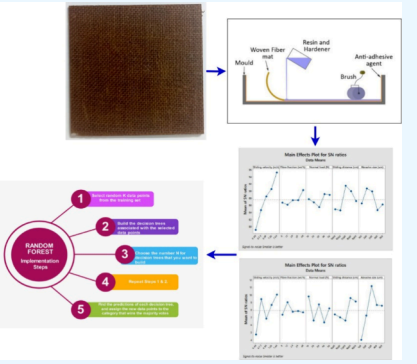


## 1. INTRODUCTION

The evolution of composites made of polymers and their ability to comply with the specified characteristics have made industries, researchers, and engineers pay high attention to it. Natural fiber polymer composites (NFPCs), too, have found their niche in the global market. The performance, relatively reduced cost, and the need for lighter parts or components have influenced the growth in the usage of NFs in the manufacturing of composites.[1] Nevertheless, it is observed from several studies that certain parameters of natural fibers (NFs), such as their durability, hydrophilicity,[2] and stability toward thermal applications, have barred their full-scale utilization in high-end applications.[3] To face such limitations, researchers have focused on obtaining the optimum benefit of a composite material by various approaches such as surface modification of the fibers, varying the lengths of fibers, hybridization, adding filler materials, weaving the fibers with different patterns, and so on.[4,5] One such approach is the plain weaving of NFs, which improves the mechanical and frictional features of the composite, which is of paramount importance to implement in tribological applications.[6−8] Complementary to the studies reported by various authors, the woven composites have exhibited explicit mechanical behaviors in orthogonal directions under various tests compared to the particle, short, or long fiber composites.[9,10]

According to a review article by Ivars et al.,[11] the most efficient and cost-effective method for producing composites is to use short, untreated fibers. On the other hand, it has been exposed by many researchers[12−14] that the stress transformation between long fibers (woven) and the matrix is superior to that of short and random-oriented fiber composites. When the fibers are weaved, the induced interlocking among the fibers enhances their strength to be greater than the binding strength between the fiber and the matrix. This is because the tightly attached

Received: October 17, 2023
Revised: January 12, 2024
Accepted: January 22, 2024
Published: February 5, 2024

fibers are less susceptible to pull-out, and the strength needed to overcome it should be very high.[15] Jute fiber and woven jute fiber polycomposites were examined by Khan et al.[16] The comparative study confirmed that the tensile strength, impact strength, and FS of the nonwoven jute composite were reasonably less than those of the woven one.[16] Similar behavior can be observed in the areca catechu composites reported by Lai and Mariatti.[17]

Many weaving styles are under practice, including plain, basket, leno, twill, noncrimp, etc. The weaving style and yarn size play a predominant role in modifying the characteristics of woven composites. Wahab et al. examined the mechanical features of the kenaf woven composite model and noted that the weaving style and yarn size are the parameters that affect the porosity and unit cell, which in turn contributes to the mechanical properties.[18] The study on sisal fiber resin composites by Pothan et al. reveals that the matt-type woven composites have exhibited enhanced tensile and flexural strength (FS) relative to the plain and twill-type woven ones.[19] Identical behavior is shown in several studies as well. Alavudeen et al. examined the features of NaOH and sodium lauryl sulfate-treated banana fibers and their hybrid with kenaf fiber woven composites in a thermoset matrix and observed that the plain-woven kind of hybrid composite has exhibited higher mechanical strength because of higher interlocking between the fibers relative to the twill-type woven composite.[20] Various kinds of weaving styles, viz., plain, basket, and twill, were employed in composite manufacturing, and the behavior of banana composites with an epoxy matrix was reported by Venkateshwaran et al. The improved mechanical properties were reported with the plain style woven composite as against the twill and basket type.[21]

The weaving pattern includes a definite number of fibers in certain orientations and contributes to the mechanical characteristics of the composites. The tensile features of a banana fiber epoxy composite were explored by Sapuan et al.[22] who observed that the warp direction had higher strength than the weft direction. From another report by Arulmurugan et al.[23] on woven aloe vera/flax hybrid epoxy composites, it is evident that the physical properties and the weaving pattern of aloe vera influenced the toughness of the composite. The same pattern can be seen in the paper published by Khan et al.,[16] where the woven jute fiber polycomposites exhibited higher tensile, impact, and flexural strength (FS) at the warp direction. The number of layers and the pattern of layering also significantly affect the qualities of the composite materials. The tensile and flexural characteristics of triple-layered woven jute composites were examined by Jawaid et al.[24] who reported that the layering pattern is the predominant factor that improves the mechanical properties and suggested the hybrids with two similar layers on either side of the sandwiched layer. Mohamad Hamdan et al.[25] studied the mechanical properties of various layering patterns on jute (J) and roselle (R) hybrid composites. The patterns JRRJ and RJJR recorded good tensile properties. Additionally, it is determined that the existence of an empty fraction means that the pattern has no bearing on the impact strength. Few authors investigated on plain-woven jute and the hybrid of plain-woven jute and glass fiber laminates and noted that the hybrid composites have a relatively lesser absorption of impact energy but higher damage tolerance capacity.[26,27] Balasubramanian et al.[28] studied the mechanical features of the composites made by layering the flax mat, aloe vera mat, straightened sisal natural fibers, aloe vera mat, and flax mat in sequence one above the other. Another sequence that changes the peripheral layering by aloe vera is compared to the sequence above. The sequence mentioned exhibited good mechanical properties. Santhanam et al.[27] examined the impact of the sequence of the banana woven. They noted that the sequence largely affected the flexural, impact strength, and water absorption characteristics and did not affect the tensile strength. According to Abdellaoui et al.,[29] the number of layers affects the mechanical characteristics of woven composites, and the optimum values are obtained for five layered composites with the 0° fiber direction and the 0° cutting direction. To check the sustainability of a new fiber of aloe vera, Kumar et al.[30] experimented with the mechanical properties of woven aloe vera fiber hybrid epoxy composites manufactured through a hand layup process. From the study, it is observed that the aloe vera and kenaf combination exhibited better flexural characteristics. The sisal and kenaf combination exhibited better tensile strength, and the composite of aloe vera, kenaf, and sisal exhibited a better impact strength. Natural silkworm silks were utilized as a reinforcement to boost impact toughness and give epoxy resin subambient qualities. Silk fibroin from *Bombyx mori* silk was combined with an epoxy resin polymer system to study molecular interactions at the silk fiber−matrix interface.[31] Zhang et al.[32] investigated steel fiber-reinforced concrete (SFRC), ordinary concrete (OC), and carbon fiber-reinforced plastic (CFRP) plates to create a composite beam. Tests examined the flexural behavior of eight specimens comprising four CSOCBs and four SFRC-OC composite beams. SWCNHs/CNFs were synthesized via electrospinning and $N_2$ annealing, and their structure was characterized using SEM, TEM, and XPS.[33] Three epoxy resin matrices with different cross-linking structures were reinforced with *Bombyx mori* silk. With its exceptional ductility and toughness, the epoxy resin made from bisphenol A epoxy and aliphatic diamine precursors produced SFRPs with the most significant impact strength (110 $kJ{\cdot}m^{-2}$) and tensile breaking energy (14.1 $MJ{\cdot}m^{-3}$). The predominant toughening methods, which enhanced specific energy dissipation during fracture processes, were crack propagation and fiber pull-out, regardless of the kind of matrix.[34] The membranes are made of electrospun polylactic acid (PLA) and PLA that has been broken down by enzymes (ED-PLA). Following enzymatic breakdown, SEM images revealed an increased fiber diameter and porosity, suggesting a particular PLA degradation pattern. Under identical conditions, PLA outlasted ED-PLA in friction tests.[35]

Because of their remarkable mechanical qualities, corrosion resistance, and simplicity of manufacture, epoxy composites have emerged as versatile materials with numerous uses in various sectors.[36] In recent years, they have been used in biomedical engineering, where materials must fulfill high biocompatibility and performance demands. Biomedical engineering is a multidisciplinary area that applies engineering principles and materials to developing medical devices, diagnostics, and therapeutics.[37] The selection of materials that interact positively with biological systems is critical to the success of biomedical engineering. Epoxy composites have gained popularity in biomedical applications because of their unique mix of mechanical strength, durability, and biocompatibility.[38] These composites have been found to be used in a variety of areas of healthcare, including orthopedics, dental prostheses, and tissue engineering.[39]

Machine learning (ML) is vital in investigating and optimizing fiber-reinforced epoxy composites (FRECs). ML approaches are useful for evaluating large data sets, predicting material behavior, improving composite qualities, and speeding up the creation of


https://doi.org/10.1021/acsomega.3c08164
ACS Omega 2024, 9, 8019−8036

novel materials.[40,41] By identifying the optimal mix of fibers, epoxy resin, and other additives, ML algorithms can aid in the design and optimizing FRECs. These algorithms may examine material attributes, processing circumstances, and cost limitations to recommend formulations that satisfy specific needs.[42] Based on the composition and processing factors, ML models may predict the mechanical, thermal, and tribological characteristics of FRECs. Based on the fiber type, orientation, volume fraction, resin parameters, and processing circumstances,[43] ML may forecast material attributes such as tensile strength, flexural strength, impact resistance, and thermal conductivity.[44] In the outer groove rolling process for a profile ring, the deformation coefficient of the cross-sectional profile per revolution was introduced, demonstrating its fluctuation under various conditions. A mathematical model was developed for this coefficient. Through simulation and testing, the model was validated for the profile ring with an exterior groove using a constructed target forged ring.[45] Using a systematic approach, the research improved arrangement patterns for 3D honeycomb and 3D re-entrant honeycomb structures. A novel sample multiplication method cut time consumption by half (93.75%). With the suggested organization pattern, simulations and testing showed a 43% improvement in energy absorption capacity under similar lateral displacement.[46] A novel high-order nonlinear friction model with spatial distribution features was developed for magnetorheological materials. Three magnetorheological material types were used to develop and validate the hysteresis dynamic model, which included nonlinear forces and demonstrated a high signal-to-noise ratio and outstanding prediction accuracy.[47] To obtain desired material qualities while reducing production costs,[48] ML algorithms may improve the manufacturing process of FRECs by altering factors such as curing time, temperature, and pressure.[49] ML speeds up creating new materials with superior performance characteristics for various applications,[50] including aerospace, automotive, biomedical, and beyond.[51]

The literature review revealed that the woven mat composites exhibit very promising and improved mechanical properties compared to the nonwoven type. The researchers are interested in optimizing the natural fiber's properties by introducing variations in weaving, layering, sequencing, proportion, and so on to find its potential usage in a particular application to replace the synthetic fiber as much as possible. Woven composites from hemp, coconut, bamboo, kenaf, flax, sisal, ramie, rice husks, bagasse, areca fruit husks, and many other natural fibers have been investigated and reported. Very limited work was reported while applying ML to predict the SWR and COF.

In light of the investigation mentioned above, it is clear that the tribological and mechanical behavior of an areca sheath fiber (ASF) composite has not received much attention. The current effort thus concentrates on the areca sheath fiber composite. The physical and mechanical properties were studied and reported. The wear behavior of the composites under the three-body wear test, where the experiments are optimized through the Taguchi approach, is reported. The ML algorithm RF is applied to model the SWR and COF. The results are investigated through the mean, SNR, and analysis of variance (ANOVA). Further to it, the worn surface of the abraded composite samples is discussed. This study is very important to determine the composite application in wear-exposed structures. So, the primary objectives of this study are as follows:

- To fabricate and evaluate woven ASF composites with varying fiber fractions in epoxy matrices.
- To investigate the tribological responses of ASF composites through three-body abrasion wear testing.
- To examine the impact of the fiber fraction on mechanical and physical properties, including density, void fraction, tensile strength, modulus, flexural strength, surface hardness, and impact strength.
- To develop and validate a machine learning predictive model, explicitly using the random forest algorithm, for forecasting the specific wear rate and coefficient of friction.

This study's relevance is multifaceted, extending into numerous major areas of interest. For starters, it meets the essential worldwide requirement for environmentally friendly materials. This study contributes to the global drive to produce sustainable and biodegradable materials by investigating woven ASF composites as environmentally benign alternatives to synthetic fibers. Sustainability is critical because it meets the growing need for environmentally sensitive solutions across several industries. Second, this research adds to the field of material innovation. It dives into ASF composites' mechanical characteristics and tribological reactions, providing material scientists and engineers with significant insights. This research's findings enable experts to design and manufacture high-performance composites that can change the construction, automotive, and packaging sectors. These observations can potentially develop more durable, efficient, and sustainable materials.

Furthermore, using data-driven methodologies, notably, the RF model, represents a significant advancement in materials research. This feature exemplifies the strength and promise of machine learning and predictive modeling. Researchers may create more precise and informed predictions regarding material qualities and performance by employing data-driven methodologies, offering new options for innovation and optimization. Finally, the multidisciplinary nature of this work contributes significantly to its significance. It successfully connects the conventional world of materials science to the new world of data-driven science. This multidisciplinary approach applies not only to the domains of materials science and engineering but also to chemistry. This interdisciplinary collaboration fosters collaboration and advances knowledge at the junction of several domains, resulting in a more comprehensive understanding of the materials and their behavior.

## 2. EXPERIMENTAL SECTION

**2.1. Materials.** The matrix phase in the current study was LY556 epoxy resin, having a density of 1.15 g/cm$^3$, and the hardener HY-951, both of which were procured from Yuje Enterprise, Bengaluru. The composite's discontinuous phase in ASF was obtained from the store of Go-green products in Tamil Nadu, India. The fiber length ranged from 820 to 1400 mm, and the diameter ranged from 400 to 700 $\mu$m. From the chemical constituent's quantification tests, the major ingredients like cellulose, hemicellulose, and lignin were observed to be 65.02, 8.26, and 18.62 wt %, respectively. The linear density of the fiber was projected to be 0.90 g/cm$^3$, consistent with the ASTM-D1577-01 standards. According to ASTM D3822-07 standards, the tensile strength, Young's modulus, and the elongation at break were 59.62 $\pm$ 2.20 MPa, 1.24 $\pm$ 0.12 GPa, and 3.02 $\pm$ 0.36%, respectively. The longer areca sheath fibers were woven


https://doi.org/10.1021/acsomega.3c08164
ACS Omega 2024, 9, 8019−8036

similarly to plain fabric, as displayed in Figure 1. The composite samples were fabricated using the hand layup method. The

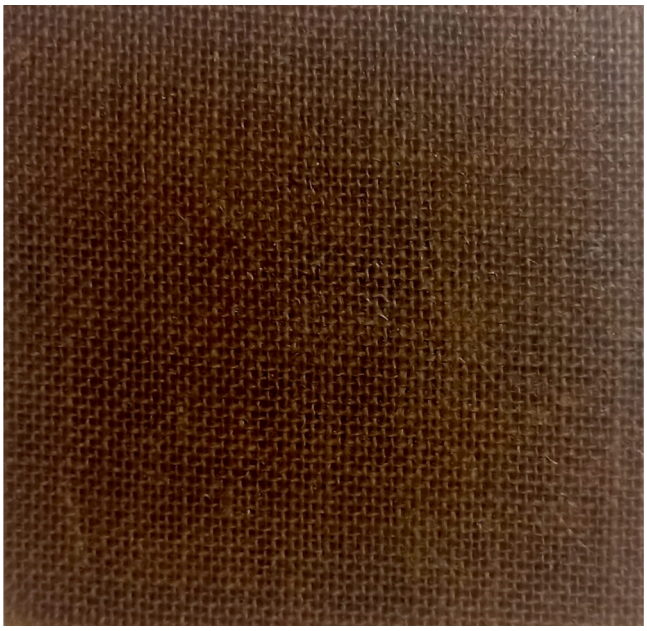

**Figure 1.** Plain-woven areca sheath fiber composite.

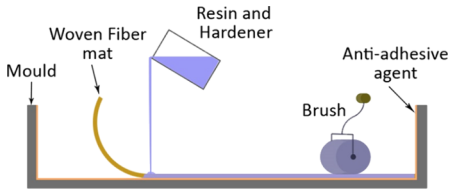


**Figure 2.** Hand layup process.

schematic of this technique is shown in Figure 2. In this technique, the mold surface was applied with an antiadhesive agent, which prevented the polymer from clinging to the surface of the mold. Then, the layers of woven areca sheath fiber reinforcements were cut into the required size and placed inside the mold layer by layer while adding the measured quantity of the matrix. The matrix of epoxy (LY556, density: 1.15 g/cm$^3$) and the hardener HY-951 mixed at suitable proportions was infused onto these layers, and a brush was used to spread the matrix uniformly on the entire surface of the reinforcement. The composite boards of varied fiber loadings were manufactured as in 0, 12, 24, 36, and 48 wt %. The molding machine, compression type (Santec), was employed for the manufacturing of composites at a pressure of 40 atm and for 24 h, which were designated as M0, M12, M24, M36, and M48, respectively. All the composite specimens were cured for 15 days followed by the physical and mechanical characterization consistent with ASTM guidelines. An average of five test runs was reported.

**2.2. Procedures.** *2.2.1. Density and the Void Fraction of Composite Materials.* Physical characteristics are just as important as mechanical features in determining whether a composite material is suitable for certain applications. The density is one of them. The theoretical density ($T_d$) of the composite samples (25 mm × 25 mm × 4 mm) with respect to their weight fraction is determined by eq 1 according to ASTM D2734-94 (2003).

$$T_d = \frac{100}{\frac{R}{D} + \frac{r}{d}} \tag{1}$$

where $T_d$ is the theoretical density, g/cm$^3$; $R$ is the weight fraction of resin; $D$ is the density of resin, g/cm$^3$; $r$ is the weight fraction of fiber; $d$ is the density of fiber, g/cm$^3$.

The composite material's actual (measured) density ($M_d$) is determined by dividing the weight by the volume. The composite void fraction ($V$) is calculated using eq 2 according to ASTM D2734-94 (2003).

$$V = \frac{100(T_d - M_d)}{T_d} \tag{2}$$

where $V$ is the void fraction, volume %; $T_d$ is the theoretical density of composites, g/cm$^3$; $M_d$ is the actual (measured) density of composites, g/cm$^3$.

*2.2.2. Mechanical Characteristics.* The Rockwell method was employed in line with ASTM D785 standards to measure the hardness of the samples with dimensions of 30 mm × 30 mm × 6 mm. The indenter used was of 0.125 in. radius. The composite's TS was determined using digital universal testing equipment (Mecmesin 2.5 *xt*) in accordance with ASTM D3039M standards. The examination was carried out on the sample of 250 mm × 25 mm × 3.2 mm size under a cross-head speed of 2 mm/min.

According to ASTM D790-03, a sample with dimensions of 150 mm × 15 mm × 3.5 mm was put through three-point flexural testing at a cross-head speed of 1.5 mm/min. The cross-head motion was calculated using eq 3.

$$R = \frac{ZL^2}{6d} \tag{3}$$

where $L$ is the span between the supports, mm; $d$ is the sample thickness, mm; $Z$ is the rate of training of the outer fiber, mm/mm/min, which will be equal to 0.0. Further to it, a short beam testing method was employed to study the ILSS. The equations used to calculate the flexural strength (FS) and ILSS are given in eqs 4 and 5, respectively.

$$\mathrm{FS} = \frac{3FL}{2wt^2} \tag{4}$$

$$\mathrm{ILSS} = \frac{3F}{4wt} \tag{5}$$

where $F$ is the maximum force applied; $L$ is the specimen length; $w$ is the specimen width; $t$ is the specimen thickness.

On a Tinius Olsen impact resistance tester machine (IT 503), the Izod impact experimentation procedure was used to evaluate the impact strength in accordance with ASTM D256 standards (sample size: 65 × 10 mm$^2$; velocity of the pendulum: 3.5 m/s; height of the pendulum: 609.6 mm).

*2.2.3. Functional Characteristics of the Specimens under the Three-Body Abrasion Wear Test.* On the rubber wheel abrasion test rig DUCOM TR50, a three-body abrasive wear test was done on the composite sample (25 mm × 76 mm × 6 mm) consistent with ASTM G65 standards. The revolution per minute (RPM) was kept at 200, and the sand flow rate (g/min) was kept at 250 g/min. The wheel of rubber employed was 228.6 mm in diameter. The abrasive, dry sand (silica sand) samples with particle sizes of 500, 400, 300, 200, and 100 $\mu$m were


https://doi.org/10.1021/acsomega.3c08164
ACS Omega 2024, 9, 8019−8036

utilized. The applied normal load differed from 10 to 50 N, stepping by 10, with sliding distances ranging from 50 to 90 m in increments of 10. The range of sliding velocity was between 0.48 and 1.44 m/s in increments of 0.24. The SWR was found out by eq 6.

$$\mathrm{SWR} = \frac{\Delta M}{\rho S F}(\mathrm{mm}^3/\mathrm{N\ m}) \tag{6}$$

where $\Delta M$ is the change of the mass of the sample (g), $\rho$ is the actual density of the sample (g/mm$^3$), $S$ is the sliding distance (m), and $F$ is the normal load (N) applied.

*2.2.4. Taguchi's Method.* The deployment of the approach intended by Taguchi is being widely applied by researchers, scientists, and others to get it right for the first time. If a process is reliable, then the outcome is dependable. The Taguchi technique proposes three layers of understanding of the design process. Level one is the system design, which looks into the basic factors that cause the desired output.[52] The emphasized second level is the parameter design, which intends to minimize variation from the target by establishing very pertinent optimal parameters covering all the basic factors.[53] The third level is the tolerance design, intended for the needed level of variation by identifying the sensitive elements affecting the product quality.[54] As a result, the technique aids in determining which process parameters are crucial to improving product quality, which parameters should be modified, the level at which process criteria should operate, and what needs to be improved and rigorously controlled. Signal-to-noise ratio (SNR) optimization is promoted to achieve process or product performance optimization by lowering the noise and enhancing the mean performance.[55] When uncontrolled noise elements are present in the system, the SNR is regarded as the experiment's output. An adequate orthogonal array is built based on the Taguchi approach, considering all of the control elements for the wear test experiment.[56,57]

From similar studies, it was observed that the control parameters like the fiber fraction ($F_F$), sliding distance ($S_D$), velocity ($V_S$), vertical load ($N_L$), and abrasive particle size ($A_S$) of abrasion material employed all influence wear characteristics.[58] The influences of the five factors as mentioned earlier on the wear characteristics are studied using the $L_{25}$ orthogonal array.[59] Table 1 depicts the experimental parameters for the wear tests conducted at laboratory temperature. Table 2 presents the $L_{25}$ orthogonal array and a combination of experimental parameters.

The responses or outputs of the experiments conducted were interpreted using the signal-to-noise ratio. SNR appraisal may consider the quality parameters STB (smaller-the-better), LTB (larger-the-better), and NTB (nominal-the-better). The goal of this research is to reduce the SWR and COF; therefore, the SNR pertaining to the STB value attributes was chosen, which can be calculated using eq 7.[60,61]

$$\mathrm{STB}: \frac{S}{N} = -10 \log \frac{1}{n}(\Sigma y^2) \tag{7}$$

In the above equations, "$n$" implies the number of tests, and "$y$" implies the observed factors.

*2.2.5. Morphological Aspects.* The surface morphology of the woven areca sheath fiber composite specimens was explored using SEM. A thin film of vacuum-evaporated platinum was applied to the surface to improve the specimen conductivity.[62]

**Table 1. Experimental Parameters for the Wear Test**

| controlled factors | variable levels | | | | |
|---|---|---|---|---|---|
| | 1 | 2 | 3 | 4 | 5 |
| VS | 0.48 m/s | 0.72 m/s | 0.96 m/s | 1.20 m/s | 1.44 m/s |
| FF | 0 wt % | 12 wt % | 24 wt % | 36 wt % | 48 wt % |
| NL | 10 N | 20 N | 30 N | 40 N | 50 N |
| SD | 50 m | 60 m | 70 m | 80 m | 90 m |
| AS | 100 $\mu$m | 200 $\mu$m | 300 $\mu$m | 400 $\mu$m | 500 $\mu$m |

**Table 2. Design of Experiments with the $L_{25}$ Orthogonal Array**

| experiment no. | VS (m/s) | FF(wt %) | NL (N) | SD (m) | AS ($\mu$m) |
|---|---|---|---|---|---|
| 1 | 0.48 | 0 | 10 | 50 | 100 |
| 2 | 0.48 | 12 | 20 | 60 | 200 |
| 3 | 0.48 | 24 | 30 | 70 | 300 |
| 4 | 0.48 | 36 | 40 | 80 | 400 |
| 5 | 0.48 | 48 | 50 | 90 | 500 |
| 6 | 0.72 | 0 | 20 | 70 | 400 |
| 7 | 0.72 | 12 | 30 | 80 | 500 |
| 8 | 0.72 | 24 | 40 | 90 | 100 |
| 9 | 0.72 | 36 | 50 | 50 | 200 |
| 10 | 0.72 | 48 | 10 | 60 | 300 |
| 11 | 0.96 | 0 | 30 | 90 | 200 |
| 12 | 0.96 | 12 | 40 | 50 | 300 |
| 13 | 0.96 | 24 | 50 | 60 | 400 |
| 14 | 0.96 | 36 | 10 | 70 | 500 |
| 15 | 0.96 | 48 | 20 | 80 | 100 |
| 16 | 1.2 | 0 | 40 | 60 | 500 |
| 17 | 1.2 | 12 | 50 | 70 | 100 |
| 18 | 1.2 | 24 | 10 | 80 | 200 |
| 19 | 1.2 | 36 | 20 | 90 | 300 |
| 20 | 1.2 | 48 | 30 | 50 | 400 |
| 21 | 1.44 | 0 | 50 | 80 | 300 |
| 22 | 1.44 | 12 | 10 | 90 | 400 |
| 23 | 1.44 | 24 | 20 | 50 | 500 |
| 24 | 1.44 | 36 | 30 | 60 | 100 |
| 25 | 1.44 | 48 | 40 | 70 | 200 |

## 3. RESULTS AND DISCUSSION

**3.1. Density and Void Fraction of Composites.** The void fraction with regard to the measured and theoretical densities of the woven fiber areca sheath composites is given in Table 3. Air bubbles may become entrapped during the production of natural fiber-reinforced composites (NFRCs), resulting in voids. The other cause for these voids' formation is the hygroscopic nature of the fiber, which gets released in the denser matrix medium. Mechanical properties are affected due to the presence of these voids, as the fibers in the region of voids shall possess

**Table 3. Density and Void Fraction of the Specimen Samples (M0 to M48)**

| specimen nomenclature | theoretical density ($T_d$) in g/cm$^3$ | measured density ($M_d$) in g/cm$^3$ | void fraction ($V$) in % |
|---|---|---|---|
| M0 | 1.150 | 1.147 | 0.261 |
| M12 | 1.1468 | 1.0905 | 4.91 |
| M24 | 1.1437 | 1.089 | 4.783 |
| M36 | 1.1405 | 1.095 | 3.978 |
| M48 | 1.1374 | 1.0935 | 3.86 |



https://doi.org/10.1021/acsomega.3c08164
ACS Omega 2024, 9, 8019−8036

Table 4. Mechanical Properties of the Specimens (M0 to M48)

| specimen | hardness (HRB) | tensile strength (MPa) | tensile modulus (GPa) | flexural strength (MPa) | flexural modulus (GPa) | impact strength IS (J/m) | interlaminar shear strength ILSS (MPa) |
|---|---|---|---|---|---|---|---|
| M0 | 40.23 | 43 | 0.15 | 45.16 | 2.25 | 52.06 | 1.02 |
| M12 | 68.26 | 68.26 | 0.68 | 26.84 | 0.524 | 28.02 | 2.84 |
| M24 | 74.86 | 88.68 | 2.88 | 34.52 | 0.682 | 42.64 | 3.86 |
| M36 | 78.62 | 96.82 | 3.24 | 50.96 | 1.18 | 56.24 | 4.26 |
| M48 | 84.26 | 104.46 | 4.22 | 52.84 | 2.86 | 64.26 | 4.68 |

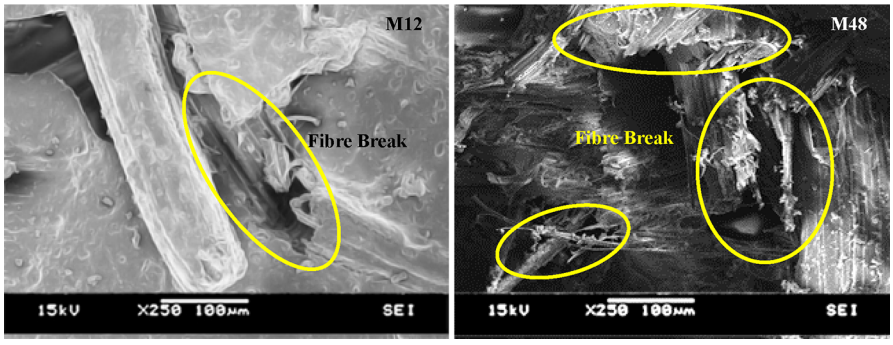


**Figure 3.** SEM images under tensile failure for M12 and M48 samples.

reduced interfacial strength. The instance of abrasion between the exposed fibers may cause the fracture of the fiber, which results in crack initiation and propagation. From Table 3, it is evident that specimen M0, the neat epoxy, has only 0.261% of voids, which increased to 4.91% in M12. The additional increase in the fiber fraction (up to 48 wt %) led to a drop in the void fraction by up to 3.86%.

The observed decrease in the void fraction with an increase in the fiber fraction in the woven fiber areca sheath composites can be attributed to several factors. As depicted in Table 3, increasing the proportion of fibers in woven natural fiber composites (12 to 48 wt %) where the fibers are properly aligned reduces the amount of voids or empty spaces between the fibers. This is primarily caused by increased fiber packing density and the matrix material's viscosity, enhanced interaction between the fiber and the matrix, and decreased shrinkage and warping during the curing process. The higher fiber content results in more fibers being incorporated into the composite material. This increased presence of fibers occupies a greater volume within the matrix, thereby reducing the overall space available for voids.[63] Consequently, the composite exhibits a denser arrangement of materials, leading to a lower void fraction. The increase in the fiber fraction may contribute to improved packing efficiency within the composite structure. The increased interlocking of fibers could leave fewer spaces for air bubbles or voids to be trapped during production. This enhanced packing efficiency further reduces the void fraction as the fiber content increases.[64]

Additionally, the text mentions that air bubbles may become trapped during the production of NFRCs. With a higher fiber fraction, there might be a decrease in the likelihood of air bubbles trapped within the matrix. The increased presence of fibers and the resulting denser arrangement could limit the opportunities for air entrapment, further influencing the reduction in the void fraction observed in the composites.[65]

**3.2. Mechanical Features of Composites.** The mechanical features of the composites, including their tensile strength (TS), flexural strength (FS), flexural modulus (FM), hardness, and impact strength (IS), are shown in Table 4. From 40.23 HRB for neat epoxy (M0) to 84.26 HRB for 48 wt % (M48) specimens, the hardness of the specimen improves. The rise in hardness of the specimens is visible since hardness depends on the relative volume concentration of the fiber and modulus. The amount of fiber content influences the improvement of tensile strength and the modulus of elasticity in the composite specimen. As the fiber content rises, the fibers prevent the dislocation shift and limit plastic deformation, improving the tensile strength and elastic modulus. From the microstructural investigation presented in Figure 3, it is evident that there was a strong interfacial interaction between the fibers and the matrix, resulting in increased tensile strength values. The primary failure mode identified was fiber breakage, which suggests strong adhesion between the fibers and the matrix. The neat epoxy's tensile strength and tensile modulus are 43.0 and 150 MPa, respectively. Estimates for the same for the areca sheath fiber woven mat are getting elevated up to 104.46 and 4220 MPa for the M48 specimen having the larger fiber fraction of 48 wt %.

The short beam testing method is employed to study the ILSS. Table 4 depicts the FS and modulus characteristics for the different woven mat areca sheath fiber specimens M0 to M48. The neat epoxy (M0) has exhibited 45.16 and 2250 MPa for the FS and the flexural modulus, respectively. On the other hand, the specimen with a 12 wt % fiber fraction experienced a fall in the above-mentioned characteristics, and it is presumed that the existence of the voids and the inadequate strength at the interfacial regions cause such a descent. The specimens M24, M36, and M48 portrayed an increase in the FS and the flexural modulus. The finest values of 52.84 and 2860 MPa are recorded pertinent to the M48 woven mat areca sheath fiber composite. The geometry of the dispersed phase and the fiber fraction are the intensifying factors in the augment of the FS and flexural modulus.[66] In this study, the woven mat areca sheath fiber composite laminates were subjected to transverse stresses, and the results are recorded. The laminates usually experience interlaminar failure during transverse loading because of the air pockets entrained, inapt laying of laminae, pressure, temperature while curing, and geometry of the laminates. Table 4 depicts the ILSS of the composite specimens with distinct fiber contents. A


https://doi.org/10.1021/acsomega.3c08164
ACS Omega 2024, 9, 8019−8036

radical ascend is observed for the composite sample with fiber fraction of 12 wt % from 1.02 MPa (for neat epoxy, M0) to 2.84 MPa, which ascends progressively with the specimens with an increase in fiber concentration. The composite sample with 48 wt % fiber fraction has recorded a maximum ILSS of 4.68 MPa. Table 4 shows for impact strength analysis that the high fiber loaded specimen has absorbed significantly more energy due to the conjugation between the fibers and matrix and good resistance to sudden loading. The neat epoxy is exhibiting impact energy of 52.06 J/m. The composite sample with 48 wt % fiber fraction had the highest impact energy of 64.26 J/m.

### 3.3. Wear Behavior under the Three-Body Wear Test.

*3.3.1. Taguchi Analysis.* The trials were carried out using a Taguchi ($L_{25}$) orthogonal array, and the responses of the trials were translated into signal-to-noise ratios (SNR). The Taguchi experimental responses are presented in Table 5. The average SNR of the composite specimens was found to be 87.643 dB for the SWR and 7.952 dB for the COF.

**Table 5. Design of Experiments with the $L_{25}$ Orthogonal Array**

| expt. no. | specific wear rate SWR ($mm^3$/Nm) | signal-to-noise ratio SNR (dB) | coefficient of friction (COF) | signal-to-noise ratio SNR (dB) |
|---|---|---|---|---|
| 1 | 0.189 | 74.71 | 0.799 | 1.951 |
| 2 | 0.099 | 80.11 | 0.699 | 3.12 |
| 3 | 0.087 | 81.525 | 0.458 | 6.775 |
| 4 | 0.099 | 80.105 | 0.498 | 6.052 |
| 5 | 0.11 | 79.332 | 0.518 | 5.707 |
| 6 | 0.06 | 82.026 | 0.498 | 6.052 |
| 7 | 0.08 | 81.94 | 0.199 | 14.03 |
| 8 | 0.04 | 87.702 | 0.549 | 5.215 |
| 9 | 0.06 | 84.746 | 0.399 | 7.985 |
| 10 | 0.045 | 86.936 | 0.199 | 14.03 |
| 11 | 0.04 | 88.427 | 0.390 | 8.183 |
| 12 | 0.05 | 86.232 | 0.390 | 8.183 |
| 13 | 0.07 | 83.622 | 0.439 | 7.159 |
| 14 | 0.02 | 94.067 | 0.390 | 8.183 |
| 15 | 0.031 | 90.23 | 0.748 | 2.520 |
| 16 | 0.054 | 85.384 | 0.518 | 5.710 |
| 17 | 0.021 | 93.64 | 0.539 | 5.380 |
| 18 | 0.02 | 94.07 | 0.298 | 10.50 |
| 19 | 0.03 | 91.44 | 0.249 | 12.08 |
| 20 | 0.04 | 88.66 | 0.328 | 9.677 |
| 21 | 0.01 | 103.64 | 0.179 | 14.96 |
| 22 | 0.035 | 89.07 | 0.189 | 14.46 |
| 23 | 0.03 | 90.52 | 0.346 | 9.229 |
| 24 | 0.05 | 86.783 | 0.559 | 5.06 |
| 25 | 0.005 | 106.41 | 0.468 | 6.591 |

Figure 4 depicts the influence of controlled parameters on the composite's SWR, whereas Figure 5 depicts the influence of controlled parameters on the composite's COF. Table 6 displays the results of the Taguchi experimental analysis.

*3.3.2. Confirmatory Run to the Design of Experiment (DOE) Result.* To meet the desired response from the set of experiments conducted, we include the best predicted setting, too. To ensure the predicted response has not deviated from the response received during the experiment, it is to be confirmed. Hence, the confirmation run is conducted again with the optimal settings. From Table 6, derived from the Figure 4, to attain the desired smaller SWR, the optimal set of control factor values is reflected in one of the $L_{25}$ orthogonal array experiments (experiment number 25 in Table 2). The confirmatory run in this regard is omitted.

On the other hand, the optimal value set for the COF mentioned in Table 6 with respect to Figure 5 is not reflected in any of the $L_{25}$ orthogonal array experiments. Therefore, the confirmatory run is performed with the set of values mentioned in Table 6 for the COF. Equation 8 gives the predicted SNR for the minimal COF.

$$\eta_{COF} = \eta_S + \eta_F + \eta_N + \eta_D + \eta_A - 4\eta_m \quad (8)$$

where $\eta_S$, $\eta_F$, $\eta_N$, $\eta_D$, and $\eta_A$ are the average value of the SNR at the optimum level of the controlled parameters (i.e., $V_S$: 1.44 m/s; $F_F$: 12 wt %; $N_L$: 10 N; $S_D$: 80 m; $A_S$: 300 $\mu$m) and $\eta_m$ is the total mean of the SNR.

The response for the confirmatory run is presented in Table 7. The predicted SNR from the set of optimal values is 17.9345 dB, and the experiment recorded a value of 17.1658 dB with an error of 4.28%.

*3.3.3. Analysis of Variance (ANOVA).* Tables 8 and 9 depict the variance analysis reports for the SWR and COF, respectively. The SWR experienced an undesirable drop with the test variance $V_S$ (69.76 %). On the other hand, the COF has also experienced such a drop with the test variances, viz., $V_S$ (30.18%) and $A_S$ (47.74%). The other test variances, namely, $F_F$, $N_L$, and $S_D$, have relatively less impact on the desired outcomes.

*3.3.4. Deviation in the SWR with the Experimental Variances (Sliding Velocity, $V_S$).* The SWR variations with the change in $V_S$ are presented in Figure 6. From Figure 6, it is obvious that the neat epoxy exhibited an increase in the wear rate as the $V_S$ increased. On the other hand, the woven areca sheath fiber composites have exhibited promising behavior. The SWR is decreasing with ascending in $V_S$. The decline is presumed to be due to the lesser contact of the abrasive wheel with the specimen during the abrasion process.[8] A similar observation is reported by a few authors in their study.[67] From the curves plotted for different specimen samples (M0−M48), it is obvious that M36 has exhibited a relatively minimal SWR.

*3.3.5. Deviation in the SWR with the Experimental Variances (Normal Load, $N_L$).* Figure 7 depicts the SWR characteristics in terms of the variant $N_L$ applied during the experiment. From the curves plotted in the figure, it is obvious that the SWR pertaining to neat epoxy (M0) is getting upraised with the rise in the application of the $N_L$. The composites (M12 to M48) with different fiber contents recorded explicit behavior similar to the one reported by a few authors in their relevant study.[68] Promising SWR desired characteristics of the composite specimen M36 at an $N_L$ of 20 N are apparent from the figure. It may be presumed that the wear rate is at its extreme when the fiber content is relatively less than the proportion of matrix material, as reflected in the neat epoxy M0 specimen. The specimens M12 and M24 also exhibit similar characteristics. The cellular structure of the fiber, formation of the wedge, and higher fiber content resist the wear and result in a lesser SWR.[69] Higher integration of the matrix with the fiber will mitigate the brittle nature of the epoxy alone and may also supplement the desired lower SWR characteristics.

On the other hand, the specimen sample M48 is exhibiting a substandard SWR, which is due to the inappropriate wetting of the fibers. More fiber fractions will experience a deficient adhesion with the matrix material and at the interfacial regions, leading to undesired SWR characteristics.



https://doi.org/10.1021/acsomega.3c08164
ACS Omega 2024, 9, 8019−8036

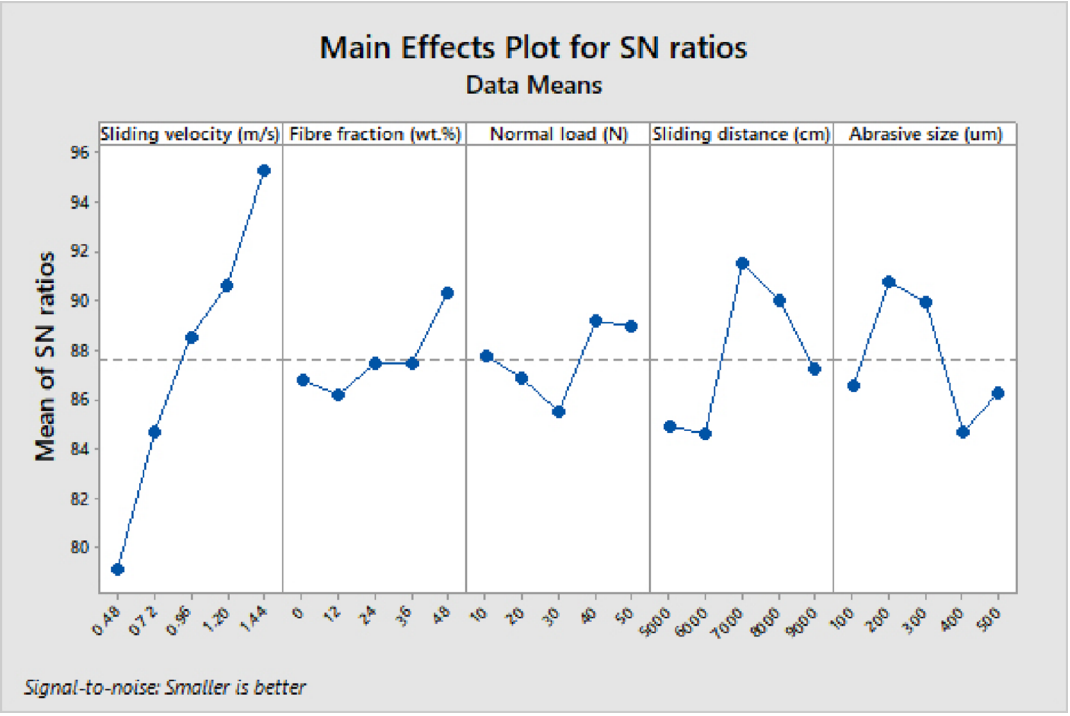


**Figure 4.** Deviation of the control factors in contemplation on the SWR of the woven composite specimens.

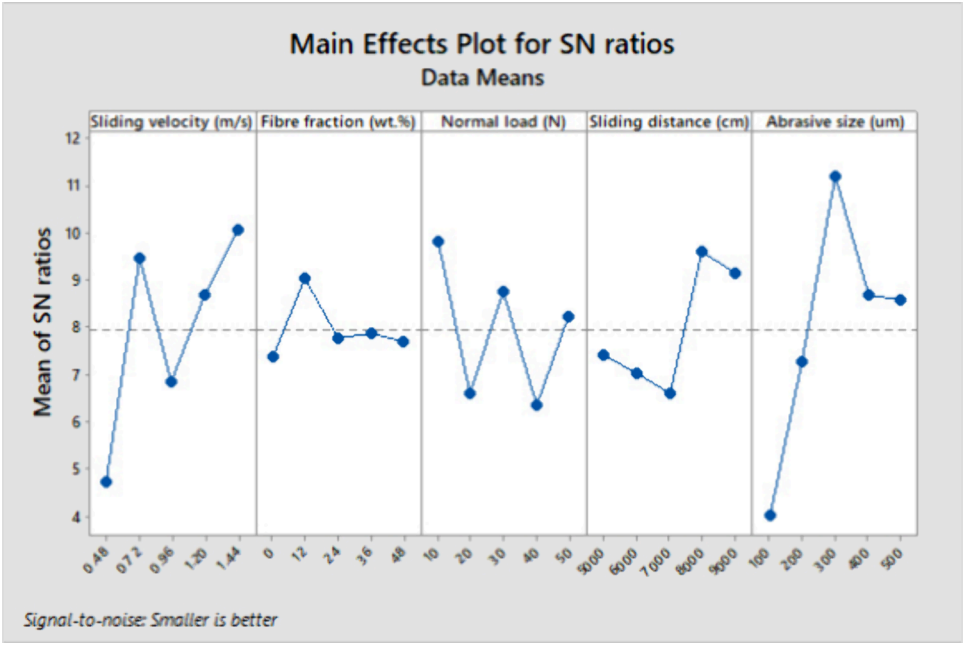


**Figure 5.** Deviation of the control factors in contemplation on the COF of the woven composite specimens.

**Table 6. Group of Process Parameters to Attain the Lowest SWR and COF**

| to attain the minimal values for the SWR (with respect to Figure 4) | to attain the minimal values for the COF (with respect to Figure 5) |
|---|---|
| $V_S$: 1.44 m/s, $F_F$: 48 wt %, $N_L$: 40 N, $S_D$: 70 m, and $A_S$: 200 $\mu$m | $V_S$: 1.44 m/s, $F_F$: 12 wt %, $N_L$: 10 N, $S_D$: 80 m, and $A_S$: 300 $\mu$m |

**Table 7. Response of the Confirmatory Run**

| SNR value for the COF in the confirmatory test run (dB) | | |
|---|---|---|
| predicted | experimental | % error |
| 17.9345 | 17.1658 | 4.28 |

*3.3.6. Deviation in the COF with the Experimental Variances (Sliding Velocity, $V_S$).* Figure 8 shows the COF variations with the variant $V_S$ applied during the wear test. The COF of any specimen, i.e., M0 to M48, begins with a minimal value and starts ascending until the $V_S$ attains 0.72 m/s. Beyond this limit of $V_S$, all the specimens with different fiber fractions (M0 to M48) exhibit an explicit behavior. The COF experiences a progressive fall as the $V_S$ increases beyond 0.72 m/s. This trend may be attributed to the increase in temperature at the interfacial



https://doi.org/10.1021/acsomega.3c08164
ACS Omega 2024, 9, 8019−8036

**Table 8. Analysis of Variance for the SWR**

| variance | DF | adj. SS | adj. MS | *F* value | *P* value | *P* (%) |
|---|---|---|---|---|---|---|
| $V_S$ (m/s) | 4 | 0.027015 | 0.006754 | 8.34 | 0.032 | 69.75573 |
| $F_F$ (wt %) | 4 | 0.002546 | 0.000636 | 0.79 | 0.590 | 6.574055 |
| $N_L$ (N) | 4 | 0.000464 | 0.000116 | 0.14 | 0.957 | 1.1981 |
| $S_D$ (m) | 4 | 0.003083 | 0.000771 | 0.95 | 0.519 | 7.960649 |
| $A_S$ ($\mu$m) | 4 | 0.002380 | 0.000595 | 0.73 | 0.614 | 6.145424 |
| error | 4 | 0.003241 | 0.000810 | | | |
| total | 24 | 0.038728 | | | | |

**Table 9. Analysis of Variance for the COF**

| variance | DF | adj. SS | adj. MS | *F* value | *P* value | *P* (%) |
|---|---|---|---|---|---|---|
| $V_S$ (m/s) | 4 | 0.20532 | 0.051329 | 14.72 | 0.012 | 30.18302 |
| $F_F$ (wt %) | 4 | 0.01808 | 0.004519 | 1.30 | 0.404 | 2.657846 |
| $N_L$ (N) | 4 | 0.07057 | 0.017642 | 5.06 | 0.073 | 10.37413 |
| $S_D$ (m) | 4 | 0.04760 | 0.011901 | 3.41 | 0.131 | 6.997427 |
| $A_S$ ($\mu$m) | 4 | 0.32475 | 0.081187 | 23.29 | 0.005 | 47.7398 |
| error | 4 | 0.01394 | | | | |
| total | 24 | 0.68025 | | | | |

region as the sliding velocity increases. In turn, thermal penetration occurs, and the polymer exhibits an elastic behavior.[70] Subsequently, the frictional force reduces with the increase in the sliding velocity.

*3.3.7. Deviation in the COF with the Experimental Variances (Normal Load, $N_L$).* Figure 9 depicts the COF variations relative to test variance $N_L$. It is obvious from the figure that the rise in the $N_L$ applied resulted in the gradual rise in the COF. Any additional normal load applied beyond it caused the declination of the COF. These characteristics can be observed in the study reported by a few authors.[70] The decline can be interpreted with the induced thermomechanical loading at higher loads, resulting in a thin layer of lubrication comprising the liquefied resin, supplemented by the lowered shear strength of the fibers at elevated temperatures.[27]

**3.4. Worn Surface Morphology.** The abrasive action at the microlevel may be because of any of the following models: the material may get displaced to the grooves formed, termed plowing; the material will get cleared from the groove, in the form of chips, termed cutting; and the material will get cracked near the groove-surrounding regions, termed as cracking.[69] To study the material wear mechanism, it is studied under a scanning electron microscope.

Worn surface morphologies of the M36 specimen at different $V_S$ of 0.48 and 1.44 m/s are presented in Figure 10a. At a $V_S$ of 0.48 m/s, the presence of wear debris and cracks and the material shift to the sides of wear grooves are evident. At a higher $V_S$, the defects described above are relatively small, even though the wear track is evident on both samples.

The morphologies of worn surfaces of the M12 specimen at $N_L$ of 10 and 50 N are presented in the below Figure 10b. Minor cracks and wear debris are evident at a lower $N_L$. The exposure of the fractured fiber, which has lost its interfacial bonding with the matrix, is clearly visible at a higher $N_L$ (50 N).

The morphologies of worn surfaces of M12 and M36 specimens are presented in Figure 10c. The surface has a smoother texture for the M36 specimen compared to the M12, which indicates less destruction of the boding of fibers at interfacial regions with the matrix. Wear debris is evident on both samples.

## 4. MACHINE LEARNING: RANDOM FOREST REGRESSION

A supervised learning approach called random forest (RF) leverages the essential properties of several decision trees to help make judgments.[71] First, during the learning phase, the RF causes the creation of sole decision tree branches. The overall prognostic is then obtained by combining the predictions from all tree branches. The ensemble learning technique is the name given to RF, which employs a set of findings to obtain a judgment. The bagging or bootstrapping technique, on which the RF is developed, is used to build a wide range of data samples from the training phase randomly chosen with replacement. Each subset of data is used to create regression trees, which are alluded to as a parallel process. As a result of its high computational cost compared with other ML methods, it is particularly effective. It is also highly precise and requires little training time. The main steps are shown in Figure 11. Combining $N$ decision trees, the first step of RF constructs the RF tree, and the second stage involves developing a proposition for every tree produced in the first stage. Finally, eq 9 computes the RF forecast.

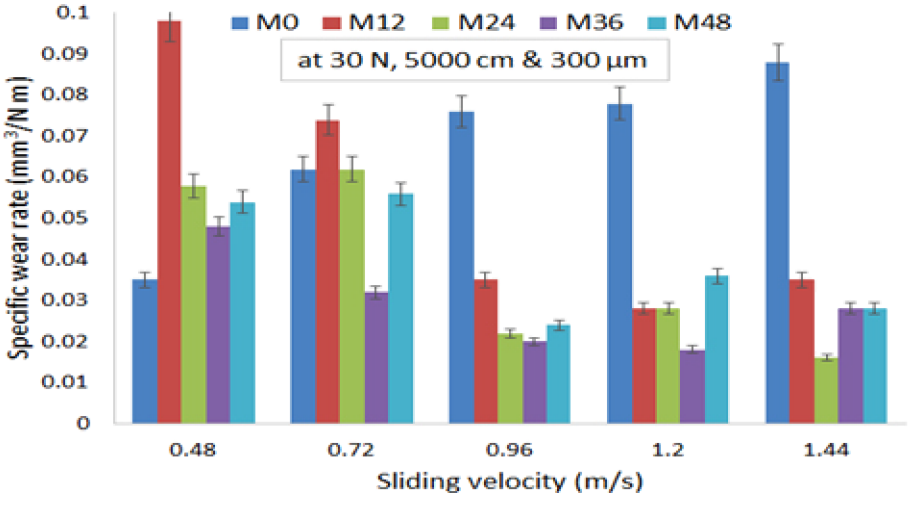


**Figure 6.** SWR variations with the experimental variance—sliding velocity ($V_S$).



https://doi.org/10.1021/acsomega.3c08164
ACS Omega 2024, 9, 8019−8036

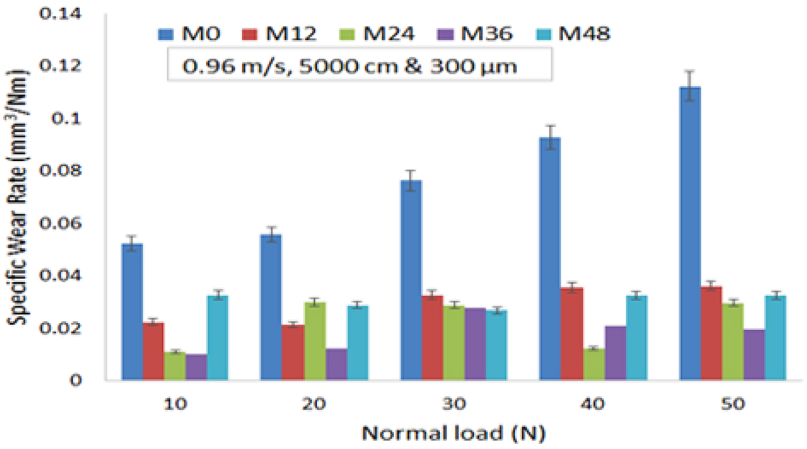


**Figure 7.** SWR variations with the experimental variance—normal load.

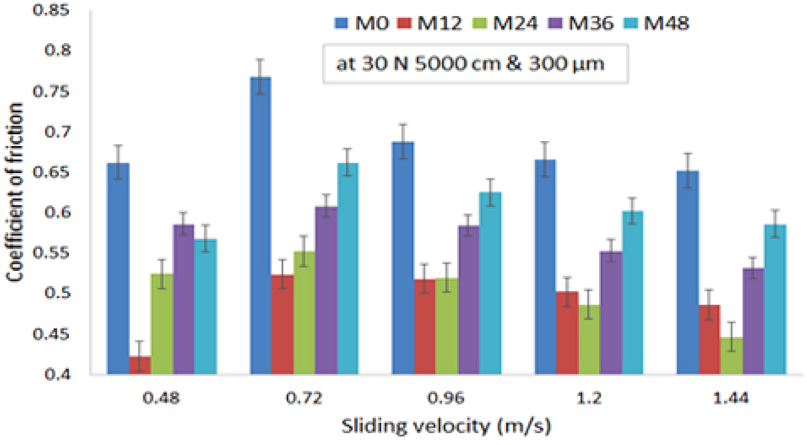


**Figure 8.** COF variations with the experimental variance—sliding velocity ($V_S$).

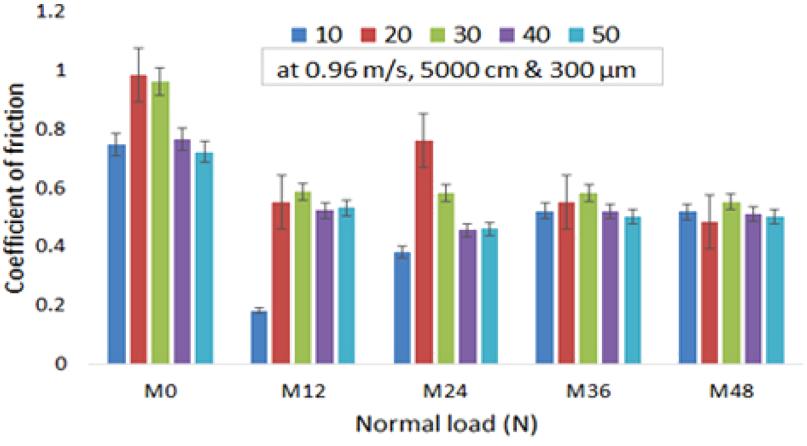


**Figure 9.** COF variations with the experimental variance—normal load ($N_L$).

$$\text{random forest prediction} = \frac{1}{J}\sum_{j=1}^{i} h_j(z) \tag{9}$$

$h_j(z)$ denotes the average of the predictions made by $J$ regression trees, and $J$ is the total number of various regression trees created for the iterations using input vector $z$.

A hyperparameter is a characteristic used to control the learning process in ML that cannot be learned via the standard training phase alone. Therefore, hyperparameters must be adjusted before the training itself begins. The complexity and learning rate of the model are two important hyperparameters. Hyperparameters in the RF increase the model's capacity for prediction or accelerate the process. The two primary hyperparameters in the RF are n_estimators, which designate how many trees are generated by the technique before optimum voting or average forecasts are made. While the computation takes longer when there are more trees, the speed is improved and forecasts are more reliable. The max_depth establishes the highest height at which a forest's trees can grow. One of the


https://doi.org/10.1021/acsomega.3c08164
ACS Omega 2024, 9, 8019−8036

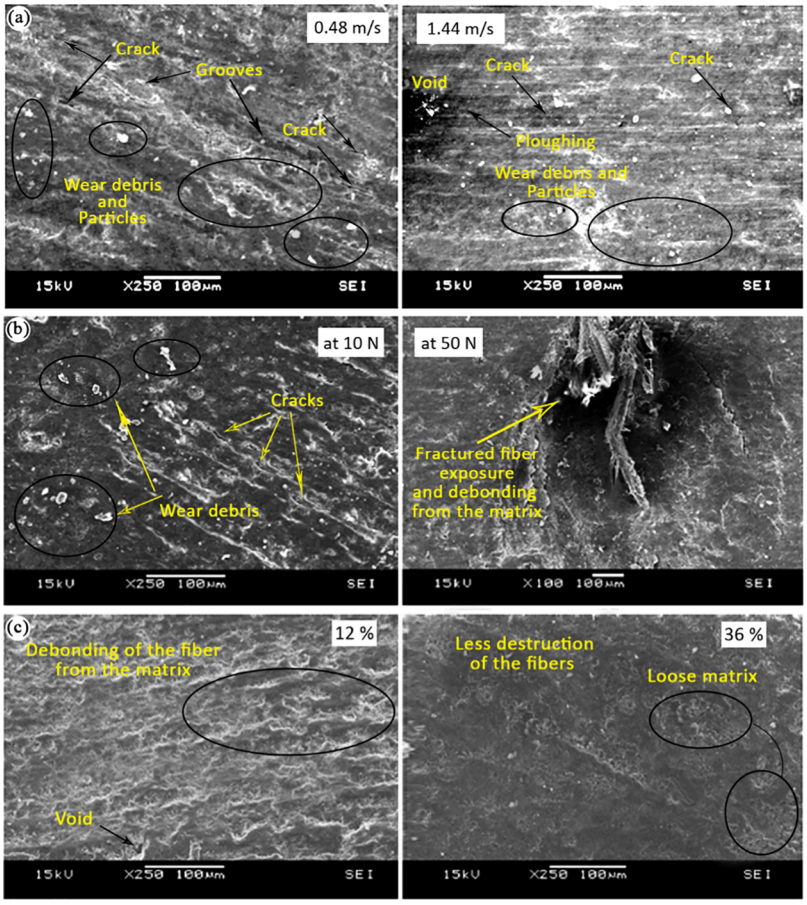


**Figure 10.** Worn surface morphology of (a) M36 specimen at a $V_S$ of 0.48 m/s and a $V_S$ of 1.44 m/s. (b) M12 specimen at an $N_L$ of 10 N and an $N_L$ of 50 N. (c) M12 and M36 composite specimens.

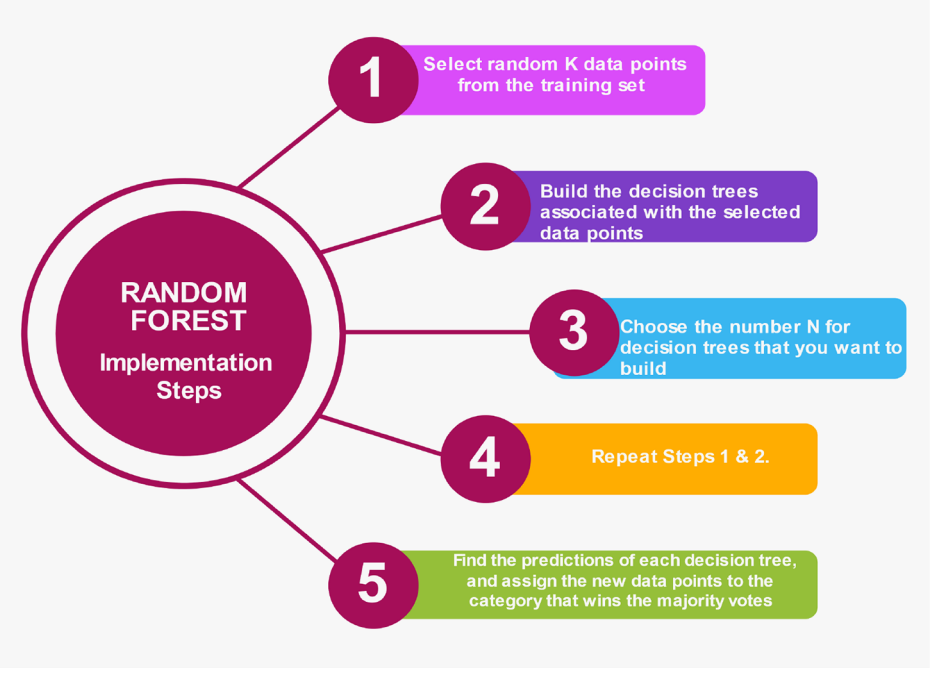


**Figure 11.** General steps of the ML algorithm: random forest (RF).

essential hyperparameters for improving model accuracy is this one.[72,73]

**4.1. Performance Evaluation Metrics for Developed ML Models.** There are various performance evaluation metrics commonly used to assess the effectiveness of the predictive ML



https://doi.org/10.1021/acsomega.3c08164
ACS Omega 2024, 9, 8019−8036

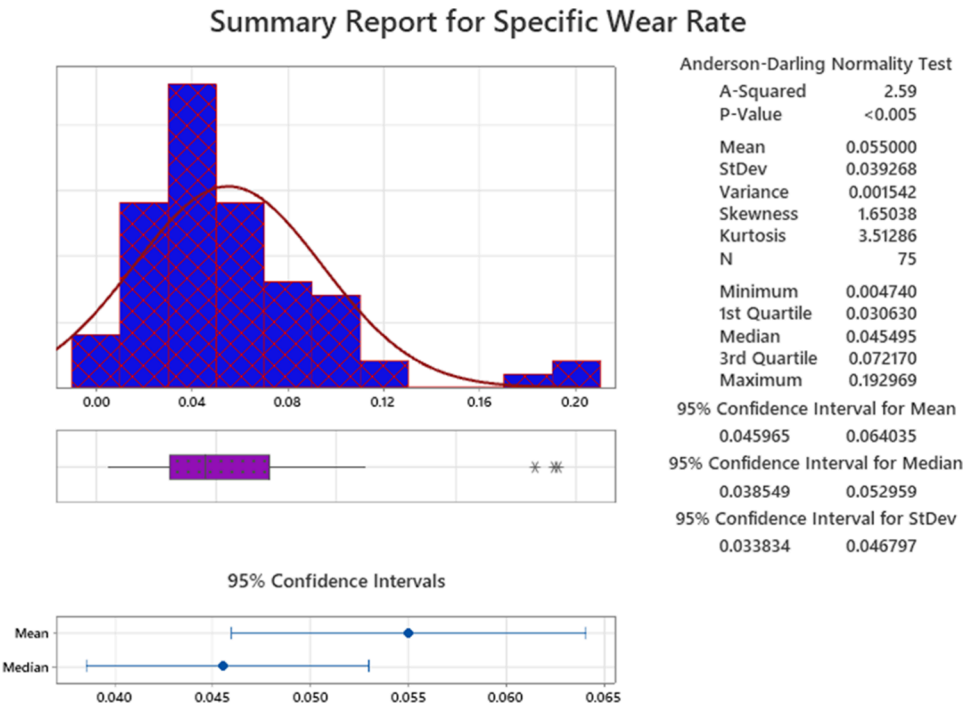


**Figure 12.** Descriptive statistics results: Anderson−Darling normality tests for the specific wear rate.

models. These metrics are essential for quantifying how well a model's predictions match the actual data. The root-mean-square error (RMSE), eq 10, measures the average square root of the squared differences between predicted values ($AN_i$) and actual values ($AV_i$). It provides a measure of the average prediction error, with lower values indicating better model performance. The mean-square error (MSE), eq 11, is similar to RMSE but without taking the square root. It measures the average of the squared differences between the predicted and actual values. Like the RMSE, lower MSE values indicate better model performance. The coefficient of determination ($R^2$), eq 12, signifies the proportion of variance in the dependent variable (actual values) that is explained by the independent variable (predicted values). It ranges from 0 to 1, with higher values indicating a better fit of the model to the data. An $R$-squared of 1 means that the model explains all of the variance, while 0 means it explains none. The mean absolute error (MAE), eq 13, measures the average absolute differences between predicted and actual values. It provides a straightforward assessment of the average prediction error, but it does not penalize large errors as strongly as RMSE. The maximum error (maxi. error), eq 14, calculates the largest absolute difference between a predicted value and an actual value. It identifies the single worst prediction in the data set. The median absolute error (MedAE), eq 15, is similar to MAE but uses the median instead of the mean to calculate the average absolute differences between predicted and actual values.[74] It is less sensitive to outliers in the data compared to mean-based metrics like MAE or RMSE.[53,75]

$$\mathrm{RMSE} = \sqrt{\frac{\sum_{i=1}^{N} (AN_i - AV_i)^2}{N}} \tag{10}$$

$$\mathrm{MSE} = \frac{1}{N} \sum (AV_i - AN_i)^2 \tag{11}$$

$$r = \frac{n(\sum xy) - (\sum x)(\sum y)}{\sqrt{\left[n\sum x^2 - (\sum^2 x)\right]\left[n\sum y^2 - (\sum^2 y)\right]}} \tag{12}$$

$$\mathrm{MAE} = \frac{1}{N} \sum |AV_i - \mathrm{AN}| \tag{13}$$

$$\text{maxi. error} = (AV_i - AN_i) \tag{14}$$

$$\mathrm{MedAE} = (|AV_i - \mathrm{median}(AV_i)|) \tag{15}$$

**4.2. Application of the Random Forest to Predict the Specific Wear Rate and the Coefficient of Friction.** The RF algorithm was employed to forecast the values of the SWR and COF. For the RF model, experimental data were used, and each experiment was conducted three times using the $L_{25}$ Taguchi orthogonal array. It is a common practice in machine learning to divide experimental data into two distinct subsets for model development and evaluation purposes. The first subset, known as the training data set, is utilized to train the model. In contrast, the second subset, referred to as the testing data set, is employed to assess the model's performance. It is customary to express the ratio of training to testing samples as a percentage, such as 90:10, 85:15, 80:20, and 70:30, with a cumulative ratio of 100%.[76] For this specific study, an 80:20 ratio was selected as the most appropriate split. In this study, the models were trained using data from 60 experimental runs, and their performance was subsequently evaluated using data from the remaining 15 runs. The experimental runs encompassed a wide range of values for process parameters, spanning the lower, middle, and higher ranges to ensure comprehensive coverage during both model training and evaluation. The RF model was implemented using Python library version 2.7.18 on a computer system with the following specifications: an 11th Gen Intel i5-1135G7 processor clocked at 2.40 GHz × 8, Mesa Intel Xe Graphics (TGL GT2),


https://doi.org/10.1021/acsomega.3c08164
ACS Omega 2024, 9, 8019−8036

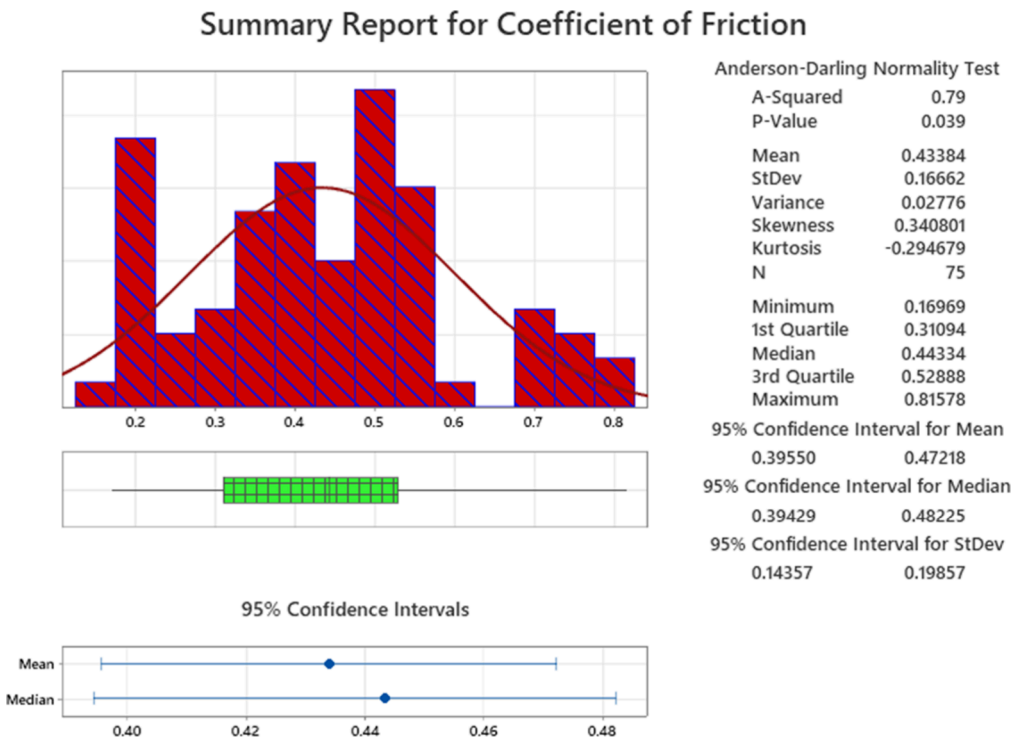


**Figure 13.** Descriptive statistics results: Anderson−Darling normality tests for the coefficient of friction.

16 GB RAM, and the Ubuntu 22.04.2 LTS 64-bit operating system.

To assess the normality of the raw data, we employed the Anderson−Darling test, a statistical technique for identifying departures from a specific probability distribution. The test is particularly effective in detecting deviations from a normal distribution when determining whether such a distribution can adequately describe the data set. Figure 12 displays the results of the Anderson−Darling normality test applied to the SWR data. The experimental data for the SWR yielded an *A*-squared value of 2.59, accompanied by a *p*-value less than 0.005. The data exhibited a mean of 0.055, a standard deviation of 0.0392, and a variance of 0.001542. The minimum observed SWR value was 0.0047 $mm^3/Nm$, while the maximum value was 0.0459 $mm^3/Nm$. Figure 13 presents the results of the Anderson−Darling test for the COF data. The raw experimental data for the COF had an *A*-squared value of 0.79, with a *p*-value of less than 0.005. The COF data displayed a mean value of 0.433, a standard deviation of 0.1666, and a variance of 0.0277. The minimum observed COF value was 0.1696, while the maximum was 0.8157.

RF regression modeling of the SWR and COF was performed based on primary hyperparameters, and random search was applied to find the best hyperparameters.

Fine-tuned hyperparameters for the SWR are as follows:

- n_estimators: 200
- min_samples_split: 2
- min_samples_leaf: 1
- max_features: log2
- max_depth: 5

Fine-tuned hyperparameters for the COF are as follows:

- n_estimators: 50
- min_samples_split: 2
- min_samples_leaf: 1
- max_features: sqrt
- max_depth: 5

The performance metrics attained are shown in Table 10. The performance metrics of the RF model were assessed for two essential parameters: the SWR and COF. The RF model performed exceptionally well in both aspects. In the case of the SWR, the model exhibited a high $R^2$ value of 0.9646, indicating that it explained approximately 96.46% of the variance in the data.

**Table 10. Performance Metrics of the RF**

| performance metric | specific wear rate | coefficient of friction |
|---|---|---|
| $R^2$ | 0.9646 | 0.9334 |
| MSE | 1.9910 | 0.0016 |
| MAE | 0.0036 | 0.0325 |
| RMSE | 0.0045 | 0.0401 |
| RAE | 1.2004 | 0.5168 |
| RSE | 0.7339 | 0.6092 |
| correlation coefficient | 0.9936 | 0.9883 |

Additionally, low MSE and MAE values of 1.9910 and 0.0036, respectively, showcased the model's ability to make highly accurate predictions with minimal errors. The COF was also predicted effectively with an $R^2$ of 0.9334 and an exceptionally low MSE and MAE of 0.0016 and 0.0325, respectively. An RSE value of 0.7339 for the SWR indicates that the model's squared errors account for approximately 73.39% of the total variation. The correlation coefficient measures the strength and direction of the linear relationship between predicted and actual SWR values. High values of 0.9936 and 0.9883 for the SWR and COF indicate a strong positive linear relationship. These results suggest that the RF model is adept at capturing and explaining the variability in both the SWR and COF, providing valuable insights and accurate predictions for these crucial parameters.



https://doi.org/10.1021/acsomega.3c08164
ACS Omega 2024, 9, 8019−8036

To gain insights into how well the model is performing, the SWR and COF models' actual versus predicted values are shown in Figure 14. In addition, 15 tests were conducted to validate the

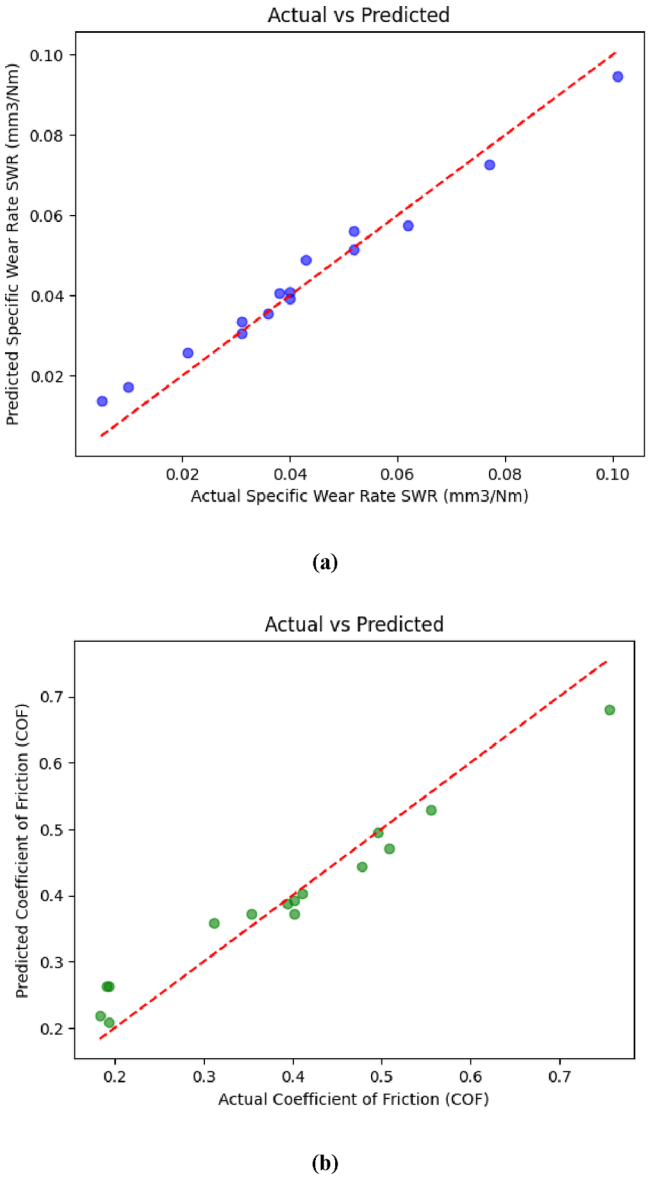


**Figure 14.** Actual vs predicted (a) SWR and (b) COF.

RF algorithm to predict SWR and COF model findings by examining the difference between the actual and predicted results. A graph was plotted with the actual SWR values on one axis and the predicted SWR values on the *y*-axis, which is known as a scatter plot. From Figure 14a for the SWR and Figure 14b for the COF, the RF model's predictions were flawless; all points almost lie on a straight line with a slope of 1 ($y = x$), representing a perfect match between actual and predicted values of the SWR and COF. Descriptive statistics for the absolute error between predicted and actual values of the SWR and COF are summarized in Table 11.

*4.2.1. Statistical Validation of the RF Model.* The statistical validation of the RF model was conducted for two performance responses, the SWR and COF, using a mean-paired *t* test.[77] The test is often used to assess whether there is a statistically significant difference between two sets of paired observations.

**Table 11. Descriptive Statistics of Absolute Error for the RF Model on the Testing Data of 20 Sets**

| statistics | absolute error SWR | absolute error COF |
|---|---|---|
| mean | 0.0036 | 0.0325 |
| SE mean | 0.0007 | 0.0063 |
| StDev | 0.0028 | 0.0243 |
| variance | 0.0000 | 0.0006 |
| CoefVar | 76.790 | 74.780 |
| minimum | 0.0003 | 0.0013 |
| Q1 | 0.0006 | 0.0094 |
| median | 0.0040 | 0.0303 |
| Q3 | 0.0060 | 0.0477 |
| maximum | 0.0089 | 0.0757 |
| range | 0.0085 | 0.0744 |

Table 12 provides descriptive statistics for the actual and predicted values of the SWR and COF.

**Table 12. Descriptive Statistics of the Actual and Predicted SWR and COF**

| sample | *N* | mean | StDev | SE mean |
|---|---|---|---|---|
| actual SWR | 15 | 0.0426 | 0.0246 | 0.0063 |
| predicted SWR | 15 | 0.0440 | 0.0210 | 0.0054 |
| actual COF | 15 | 0.3884 | 0.1609 | 0.0415 |
| predicted COF | 15 | 0.3904 | 0.1256 | 0.0324 |

Table 13 presents estimations for the paired differences between the actual and predicted values for the SWR and COF.

**Table 13. Estimation for the Paired Difference of the Actual and Predicted SWR and COF[a]**

| | estimation for the paired difference | | | |
|---|---|---|---|---|
| | mean | StDev | SE mean | 95% CI for $\mu$_difference |
| SWR | −0.00138 | 0.00439 | 0.00113 | (−0.00382, 0.00105) |
| COF | −0.002 | 0.0415 | 0.0107 | (−0.0249, 0.0210) |

[a]$\mu$_difference: population mean of (actual − predicted).

These paired differences represent how much the model's predictions deviate from the actual values. Table 14 displays the

**Table 14. Test Results: Paired *t* Tests[a]**

| | *T*-value | *P*-value |
|---|---|---|
| SWR | −1.22 | 0.242 |
| COF | −0.18 | 0.857 |

[a]Null hypothesis $H_0$: $\mu$_difference = 0; alternative hypothesis $H_1$: $\mu$_difference ≠ 0.

paired *t* test results, which assess whether the observed differences between actual and predicted values are statistically significant. The null and alternative hypotheses are as follows:

- Null hypothesis ($H_0$): $\mu$_difference = 0, meaning that there is no significant difference between actual and predicted values.
- Alternative hypothesis ($H_1$): $\mu$_difference ≠ 0, indicating a significant difference between actual and predicted values.

In the case of the SWR, the *t*-value is −1.22, and the *p*-value is 0.242. Since the *p*-value is not smaller than the typical significance level of 0.05, there is no substantial evidence to


https://doi.org/10.1021/acsomega.3c08164
ACS Omega 2024, 9, 8019−8036

reject the null hypothesis for the SWR, implying that the model's predictions are statistically similar to the actual values. For the COF, the $t$-value is −0.18, and the $p$-value is 0.857. Again, the $p$-value is not smaller than 0.05, indicating that there is no significant difference between the actual and predicted values for the COF based on the statistical test. The results of the paired $t$ test suggest that there is no statistically significant difference between the actual and predicted values for both the SWR and COF, indicating that the RF model appears to be statistically fit for these performance responses.

**4.3. Practical and Theoretical Implications.** This research has both practical and theoretical consequences for materials science and chemistry. The findings provide valuable recommendations for improving the woven ASF composites. The research provides practical insights into the construction, automotive, and packaging sectors by discovering the most advantageous fiber fraction for increasing the mechanical characteristics and tribological performance. This knowledge can be used by manufacturers and engineers to customize ASF composites to their unique needs, resulting in materials that not only are environmentally benign but also perform well in real-world applications.

Theoretically, this research contributes to a better understanding of the complex link between fiber percentage and composite characteristics. This study establishes a solid platform for further theoretical inquiry in materials science and chemistry by studying how modifying the concentration of ASF fibers affects attributes such as the density, void fraction, tensile strength, modulus, flexural strength, and impact strength. It encourages scientists and researchers to dive further into these composites' underlying chemical and mechanical interactions. The theoretical progress adds to the academic knowledge base and provides a foundation for developing new ideas and models in these disciplines. The study provides practical business answers while enhancing the theoretical background in materials science and chemistry.

## 5. CONCLUSIONS

Epoxy composites reinforced with woven areca sheath fiber at 0, 12, 24, 36, and 48% fiber fractions were tested and evaluated for their tribological responses on a three-body abrasion wear testing machine, as well as their mechanical and physical properties, and the following conclusions were drawn:

- As the fiber fraction rises, the composite's density increases from 1.1374 to 1.150 g/cm$^3$, and its void fraction rises from 0.261 to 3.8%.
- The results indicate that the composite with a 48% fiber loading possesses superior mechanical properties to the others, including a greater tensile strength (104 MPa), tensile modulus (4.22 GPa), flexural strength (52.84 MPa), surface hardness (84.26 HRB), impact strength (64.26 J), and interlaminar shear strength (4.68 MPa).
- The composite sample with a fiber weight percentage of 36 wt % (M36) exhibited a low SWR as the $V_S$ was increased and a low COF when subjected to a normal load of 20 N.
- The specimen M24, which contains 24 wt % areca sheath fibers, demonstrates the lowest COF due to the application of $V_S$ and $N_L$. In contrast to the M12 specimen, which exhibits fiber fracture, exposed fibers, wear debris, and cracks that result in poor SWR at high loads (50 N), the M36 specimen exhibits less destruction of fiber bonding with the matrix at high $V_S$, as evidenced by the morphology of the worn surfaces. Utilizing ANOVA techniques, the wear test outcomes were validated.
- The RF model demonstrates strong predictive performance for both the SWR and COF, with high $R$-squared values indicating a good fit to the data.
- For the SWR, the model has a low MSE (1.9910) and a very low MAE (0.0036), signifying accurate predictions with minimal errors. For the COF, the model also exhibits a low MSE (0.0016) and a reasonable MAE (0.0325), indicating accurate predictions with a slightly larger average error compared to the SWR.
- The statistical validation through the paired $t$ test confirms no statistically significant difference between the actual and predicted values for both the SWR ($p$-value = 0.242) and COF ($p$-value = 0.857). These quantitative results collectively suggest that the RF model is highly reliable and effective for predicting the SWR and COF.

**5.1. Limitations.** It is vital to recognize the various limitations in this study. First, while controlled laboratory settings are necessary for controlled tests, they may not fully reproduce the complex and dynamic situations that ASF composites would encounter in real-world applications. As a result, the findings should be taken with the possibility of changes in real usage and long-term material behavior in mind. Second, the intrinsic variety of natural fibers, such as woven ASF, brings an element of randomness into the outcomes. Natural materials' characteristics can change according to climate, soil conditions, and growth differences. These changes might have an effect on the consistency of the experimental results. Furthermore, while the study shows the random forest machine learning model's usefulness in forecasting the SWR and COF, it only focuses on one specific machine learning model. Future studies might look at alternative machine learning models or mix different models to grasp this sector's predictive potential better.

**5.2. Future Directions.** Several future approaches might be followed to expand on the present research and solve these constraints. One possible route is the study's expansion to analyze ASF composites' environmental effects and biodegradability. A more extensive examination can give a more comprehensive view of the sustainability of these materials and their potential environmental benefits. Furthermore, combining several machine learning models and sophisticated analytical approaches in a multimodal analysis approach might result in a more thorough knowledge of ASF composites and their characteristics. The multipronged approach has the potential to give deeper insights into the complicated interactions that occur inside these materials. Another path for future study is to investigate the practical usability of ASF composites in various sectors and undertake field tests in real-world settings. The validation method ensures that laboratory findings are efficiently transferred to practical and industrial contexts. Finally, exploring the prospects of mixing ASF with other natural or synthetic fibers to generate hybrid composites with improved characteristics is a fascinating field of research. Researchers may be able to build composites with more outstanding performance and expand application possibilities by combining diverse materials. These future avenues have the potential to enhance the area and provide remedies for the constraints observed in this study.



https://doi.org/10.1021/acsomega.3c08164
ACS Omega 2024, 9, 8019−8036

## ■ ASSOCIATED CONTENT

### Data Availability Statement

All the data used to support the findings of this study are included in the article.

## ■ AUTHOR INFORMATION


### Corresponding Authors

**Raman Kumar** − *Department of Mechanical and Production Engineering, Guru Nanak Dev Engineering College, Ludhiana, Punjab 141006, India;* orcid.org/0000-0003-2934-7609; Email: sehgal91@yahoo.co.in

**Ketan Kotecha** − *Symbiosis Centre for Applied Artificial Intelligence, Symbiosis Institute of Technology, Symbiosis International University Pune, Pune 411014, India;* Email: director@sitpune.edu.in

### Authors

**Suresh Poyil Subramanyam** − *Department of Mechanical Engineering, Alva's Institute of Engineering and Technology, Mijar, Karnataka 574225, India*

**Dilip Kumar Kotikula** − *Department of Mechanical Engineering, K S Institute of Technology, Bengaluru, Karnataka 560109, India*

**Basavaraju Bennehalli** − *Department of Chemistry, MVJ College of Engineering, Bengaluru, Karnataka 560067, India*

**Atul Babbar** − *Department of Mechanical Engineering, SGT University, Gurugram, Haryana 122505, India*

**Sagr Alamri** − *Department of Mechanical Engineering, College of Engineering, King Khalid University, Abha 61421, Saudi Arabia*

**Alaauldeen A. Duhduh** − *Department of Mechanical Engineering Technology, CAIT, Jazan University, Jazan 45142, Saudi Arabia*

**Ali A. Rajhi** − *Department of Mechanical Engineering, College of Engineering, King Khalid University, Abha 61421, Saudi Arabia*

Complete contact information is available at: https://pubs.acs.org/10.1021/acsomega.3c08164


### Notes

The authors declare no competing financial interest.

## ■ ACKNOWLEDGMENTS

The authors extend their appreciation to the Deanship of Scientific Research at King Khalid University, Saudi Arabia, for funding this work through the Research Group Program under Grant No. RGP. 2/84/44.

## ■ NOMENCLATURE

MPa = megapascal
dB = decibels
wt % = percentage by weight
HRB = hardness Rockwell B
FM = flexural modulus
TS = tensile strength
TM = tensile modulus
IS = impact strength
ILSS = interlaminar shear strength
$T_d$ = theoretical density
$M_d$ = measured density
$V$ = void fraction
DF = degrees of freedom
adj SS = adjusted sums of squares
adj MS = adjusted mean of squares

## ■ REFERENCES


(1) Karaçor, B.; ÖZCANLI, M. Examination of fiber reinforced composite materials. *Gazi University Journal of. Science* **2023**, *36* (1), 301−320.

(2) Hu, G.; Ying, S.; Qi, H.; Yu, L.; Li, G. Design, analysis and optimization of a hybrid fluid flow magnetorheological damper based on multiphysics coupling model. *Mech Syst. Signal Process* **2023**, *205*, No. 110877.

(3) Kanaginahal, G. M.; Hebbar, S.; Shahapurkar, K.; Alamir, M. A.; Tirth, V.; Alarifi, I. M.; Sillanpaa, M.; Murthy, H. C. A. Leverage of weave pattern and composite thickness on dynamic mechanical analysis, water absorption and flammability response of bamboo fabric/epoxy composites. *Heliyon* **2023**, *9* (1), No. e12950.

(4) Zhao, Y.; Jing, J.; Chen, L.; Xu, F.; Hou, H. Current research status of interface of ceramic-metal laminated composite material for armor protection. *Acta Metall Sin* **2021**, *57* (9), 1107−1125.

(5) Guo, Y.; Wang, L.; Zhang, Z.; Cao, J.; Xia, X.; Liu, Y. Integrated modeling for retired mechanical product genes in remanufacturing: A knowledge graph-based approach. *Adv. Eng. Inf.* **2024**, *59*, No. 102254.

(6) Bajpai, P. K.; Singh, I.; Madaan, J. Tribological behavior of natural fiber reinforced PLA composites. *Wear* **2013**, *297* (1), 829−840.

(7) Anand, P. B.; Nagaraja, S.; Jayaram, N.; Sreenivasa, S. P.; Almakayeel, N.; Khan, T. M. Y.; Kumar, R.; Kumar, R.; Ammarullah, M. I. Kenaf Fiber and Hemp Fiber Multi-Walled Carbon Nanotube Filler-Reinforced Epoxy-Based Hybrid Composites for Biomedical Applications: Morphological and Mechanical Characterization. *J. Compos. Sci.* **2023**, *7* (8), 324.

(8) Li, X.; Liu, Y.; Leng, J. Large-scale fabrication of superhydrophobic shape memory composite films for efficient anti-icing and de-icing. *Sustainable Materials and Technologies* **2023**, *37*, No. e00692.

(9) Aisyah, H. A.; Paridah, M. T.; Sapuan, S. M.; Ilyas, R. A.; Khalina, A.; Nurazzi, N. M.; Lee, S. H.; Lee, C. H. A Comprehensive Review on Advanced Sustainable Woven Natural Fibre Polymer Composites Polymers [Online]. *Polymers* **2021**, 471.

(10) Laqraa, C.; Labanieh, A. R.; Soulat, D.; Ferreira, M. Development of woven and quasi-unidirectional reinforcement fabrics with hemp fibers: study of mechanical and preforming behaviors. *Int. J. Mater. Form.* **2022**, *16* (1), 8.

(11) Ivars, J.; Labanieh, A. R.; Soulat, D. Effect of the Fibre Orientation Distribution on the Mechanical and Preforming Behaviour of Nonwoven Preform Made of Recycled Carbon Fibres Fibers [Online]. *Fibers* **2021**, 82.

(12) Suresh, P. S.; Dilip Kumar, K.; Dhanalakshmi, S.; Srinivasa, C. V.; Basavaraju, B. Effect of fiber fraction on the physical and mechanical properties of short areca sheath fiber reinforced polymer composite. *Materials Today: Proceedings* **2021**, *44*, 4972−4975.

(13) Arumugam, S.; Kandasamy, J.; Venkatesan, S.; Murugan, R.; Lakshmi Narayanan, V.; Sultan, M. T.; Shahar, F. S.; Shah, A. U.; Khan, T.; Sebaey, T. A. A Review on the Effect of Fabric Reinforcement on Strength Enhancement of Natural Fiber Composites Materials [Online]. *Materials* **2022**, 3025.

(14) Prashanth, M.; Gouda, P. S. S.; Manjunatha, T. S.; Banapurmath, N. R.; Edacheriane, A. Understanding the impact of fiber orientation on mechanical, interlaminar shear strength, and fracture properties of jute−banana hybrid composite laminates. *Polym. Compos.* **2021**, *42* (10), 5475−5489.

(15) Lomov, S. V.; Willems, A.; Verpoest, I.; Zhu, Y.; Barburski, M.; Stoilova, T. Picture Frame Test of Woven Composite Reinforcements with a Full-Field Strain Registration. *Text. Res. J.* **2006**, *76* (3), 243−252.

(16) Khan, G. M. A.; Terano, M.; Gafur, M. A.; Alam, M. S. Studies on the mechanical properties of woven jute fabric reinforced poly(l-lactic acid) composites. *Journal of King Saud University - Engineering Sciences* **2016**, *28* (1), 69−74.




https://doi.org/10.1021/acsomega.3c08164
*ACS Omega* 2024, 9, 8019−8036

(17) Lai, W. L.; Mariatti, M. The Properties of Woven Betel Palm (Areca catechu) Reinforced Polyester Composites. *Journal of Reinforced Plastics and Composites* **2008**, *27* (9), 925−935.
(18) Wahab, M. S.; Rejab, M. N.; Saiman, M. P. Analysis of mechanical properties for 2D woven kenaf composite. *Applied Mechanics and Materials* **2014**, *660*, 125−129.
(19) Pothan, L. A.; Mai, Y. W.; Thomas, S.; Li, R. K. Y. Tensile and Flexural Behavior of Sisal Fabric/Polyester Textile Composites Prepared by Resin Transfer Molding Technique. *Journal of Reinforced Plastics and Composites* **2008**, *27* (16−17), 1847−1866.
(20) Alavudeen, A.; Rajini, N.; Karthikeyan, S.; Thiruchitrambalam, M.; Venkateshwaren, N. Mechanical properties of banana/kenaf fiber-reinforced hybrid polyester composites: Effect of woven fabric and random orientation. *Mater. Des.* **2015**, *66*, 246−257.
(21) Venkateshwaran, N.; ElayaPerumal, A.; Arwin Raj, R. H. Mechanical and Dynamic Mechanical Analysis of Woven Banana/Epoxy Composite. *Journal of Polymers and the Environment* **2012**, *20* (2), 565−572.
(22) Sapuan, S. M.; Leenie, A.; Harimi, M.; Beng, Y. K. Mechanical properties of woven banana fibre reinforced epoxy composites. *Materials & Design* **2006**, *27* (8), 689−693.
(23) Arulmurugan, M.; Selvakumar, A. S.; Prabu, K.; Rajamurugan, G. Effect of barium sulphate on mechanical, DMA and thermal behaviour of woven aloevera/flax hybrid composites. *Bull. Mater. Sci.* **2020**, *43* (1), 58.
(24) Jawaid, M.; Abdul Khalil, H. P. S.; Abu Bakar, A. Woven hybrid composites: Tensile and flexural properties of oil palm-woven jute fibres based epoxy composites. *Materials Science and Engineering: A* **2011**, *528* (15), 5190−5195.
(25) Mohamad Hamdan, M. H.; Siregar, J. P.; Thomas, S.; Jacob, M. J.; Jaafar, J.; Tezara, C. Mechanical performance of hybrid woven jute−roselle-reinforced polyester composites. *Polymers and Polymer Composites* **2019**, *27* (7), 407−418.
(26) Ahmed, K. S.; Vijayarangan, S.; Kumar, A. Low Velocity Impact Damage Characterization of Woven Jute—Glass Fabric Reinforced Isothalic Polyester Hybrid Composites. *Journal of Reinforced Plastics and Composites* **2007**, *26* (10), 959−976.
(27) V, S.; R, D.; M, C.; N, V.; S, B. Experimental investigation on the mechanical properties of woven hybrid fiber reinforced epoxy composite. *Mater. Today: Proc.* **2021**, *37*, 1850−1853.
(28) Balasubramanian, K.; Rajeswari, N.; Vishvak, R. Influence of sequential positioning of fibre mats in enhancing the properties of natural fibre mat hybrid composite. *Materials Today: Proceedings* **2020**, *28*, 1144−1148.
(29) Abdellaoui, H.; Bensalah, H.; Echaabi, J.; Bouhfid, R.; Qaiss, A. Fabrication, characterization and modelling of laminated composites based on woven jute fibres reinforced epoxy resin. *Materials & Design* **2015**, *68*, 104−113.
(30) Kumar, K. P.; Jeya Sekaran, A. S.; Pitchandi, K. Investigation on mechanical properties of woven alovera/sisal/kenaf fibres and their hybrid composites. *Bulletin of Materials Science* **2017**, *40* (1), 117−128.
(31) Yang, K.; Yazawa, K.; Tsuchiya, K.; Numata, K.; Guan, J. Molecular Interactions and Toughening Mechanisms in Silk Fibroin−Epoxy Resin Blend Films. *Biomacromolecules* **2019**, *20* (6), 2295−2304.
(32) Zhang, W.; Kang, S.; Liu, X.; Lin, B.; Huang, Y. Experimental study of a composite beam externally bonded with a carbon fiber-reinforced plastic plate. *J. Build. Eng.* **2023**, *71*, No. 106522.
(33) Zhang, L.; Qin, D.; Feng, J.; Tang, T.; Cheng, H. Rapid quantitative detection of luteolin using an electrochemical sensor based on electrospinning of carbon nanofibers doped with single-walled carbon nanoangles. *Analytical Methods* **2023**, *15* (25), 3073−3083.
(34) Yang, K.; Wu, Z.; Zhou, C.; Cai, S.; Wu, Z.; Tian, W.; Wu, S.; Ritchie, R. O.; Guan, J. Comparison of toughening mechanisms in natural silk-reinforced composites with three epoxy resin matrices. *Composites Part A: Applied Science and Manufacturing* **2022**, *154*, No. 106760.
(35) Wang, Y.; Zhai, W.; Li, J.; Liu, H.; Li, C.; Li, J. Friction behavior of biodegradable electrospun polyester nanofibrous membranes. *Tribol Int.* **2023**, *188*, No. 108891.
(36) Khalid, M. Y.; Kamal, A.; Otabil, A.; Mamoun, O.; Liao, K. Graphene/epoxy nanocomposites for improved fracture toughness: A focused review on toughening mechanism. *Chem. Eng. J. Adv.* **2023**, *16*, No. 100537.
(37) Ahmed, P. S. Role of intra-ply hybridization and nano reinforcement on crack growth of epoxy. *Pigment Resin Technol.* **2023**, DOI: 10.1108/PRT-07-2023-0065.
(38) Oladele, I. O.; Taiwo, A. S.; Onuh, L. N.; Makinde-Isola, B. A. Microstructural features and mechanical, wear and thermal conductivity characteristics of eggshell derived hydroxyapatite reinforced epoxy bio-composites. *J. Tribol.* **2022**, *35*, 68−91.
(39) Balasubramanian, M.; Madhu, S. Effect of the threaded nozzle on delamination and surface texture of PEEK CF30 composite machined by abrasive jet. *World Journal of Engineering* **2022**, *19* (6), 755−765.
(40) Sawangsri, W.; Prasithmett, P. Concept and development of IoT-based e-maintenance platform for demonstrated system. *Int. J. Interact. Des. Manuf.* **2023**, 1.
(41) Vaddar, L.; Thatti, B.; Reddy, B. R.; Chittineni, S.; Govind, N.; Vijay, M.; Anjinappa, C.; Razak, A.; Saleel, C. A. Glass Fiber-Epoxy Composites with Carbon Nanotube Fillers for Enhancing Properties in Structure Modeling and Analysis Using Artificial Intelligence Technique. *ACS Omega* **2023**, *8* (26), 23528−23544.
(42) Mahakur, V. K.; Bhowmik, S.; Patowari, P. K. Tribo-informatics evaluation of dry sliding friction of silanized jute filler reinforced epoxy composites using machine learning techniques. *Tribol. Int.* **2023**, *183*, No. 108388.
(43) Mishra, A.; Jatti, V. S. Reinforcement learning based approach for the optimization of mechanical properties of additively manufactured specimens. *Int. J. Interact. Des. Manuf.* **2023**, *17* (4), 2045−2053.
(44) Imoisili, P. E.; Adeleke, O.; Makhatha, M. E.; Jen, T. C. Response Surface Methodology (RSM)- Artificial Neural Networks (ANN) Aided Prediction of The Impact Strength of Natural Fibre/Carbon Nanotubes Hybrid Reinforced Polymer Nanocomposite. *Eng. Sci.* **2023**, *23*, 852.
(45) Deng, J.; Wu, R.; Sun, Z.; Qian, D.; Zhang, Y. A prediction model of ultimate forming dimension for profile ring with outer groove in ring rolling process. *International Journal of Advanced Manufacturing Technology* **2024**, *130* (1), 491−510.
(46) Xia, B.; Huang, X.; Chang, L.; Zhang, R.; Liao, Z.; Cai, Z. The arrangement patterns optimization of 3D honeycomb and 3D re-entrant honeycomb structures for energy absorption. *Mater. Today Commun.* **2023**, *35*, No. 105996.
(47) Zhou, C.; Ren, Z.; Lin, Y.; Huang, Z.; Shi, L.; Yang, Y.; Mo, J. Hysteresis dynamic model of metal rubber based on higher-order nonlinear friction (HNF). *Mech Syst. Signal Process* **2023**, *189*, No. 110117.
(48) Yang, C.; Yin, C.; Wu, Y.; Zhou, Q.; Liu, X. Atomic insights into the deformation mechanism of an amorphous wrapped nanolamellar heterostructure and its effect on self-lubrication. *J. Mater. Res. Technol.* **2023**, *26*, 4206−4218.
(49) Kumar, A. K.; Surya, M. S.; Venkataramaiah, P. Performance evaluation of machine learning based-classifiers in friction stir welding of Aa6061-T6 alloy. *Int. J. Interact. Des. Manuf.* **2023**, *17* (1), 469−472.
(50) Bian, Y.; Zhu, S.; Li, X.; Tao, Y.; Nian, C.; Zhang, C.; Peng, Y.; Li, C.; Xiong, W.; Zhu, W.; Hu, Y.; Li, J.; Chu, J.; Wu, D. Bioinspired magnetism-responsive hybrid microstructures with dynamic switching toward liquid droplet rolling states. *Nanoscale* **2023**, *15* (28), 11945−11954.
(51) Divakarraju, P. V.; Mishra, N.; Pandurangan, V.; Nithyadharan, M. Machine learning based inverse framework for predicting the transverse and shear modulus of carbon fiber. *Comput. Mater. Sci.* **2023**, *230*, No. 112518.
(52) Yang, S.; Zhang, Y.; Sha, Z.; Huang, Z.; Wang, H.; Wang, F.; Li, J. Deterministic Manipulation of Heat Flow via Three-Dimensional-Printed Thermal Meta-Materials for Multiple Protection of Critical Components. *ACS Appl. Mater. Interfaces* **2022**, *14* (34), 39354−39363.
(53) Kumar, R.; Channi, A. S.; Kaur, R.; Sharma, S.; Grewal, J. S.; Singh, S.; Verma, A.; Haber, R. Exploring the intricacies of machine

learning-based optimization of electric discharge machining on squeeze cast TiB2/AA6061 composites: Insights from morphological, and microstructural aspects in the surface structure analysis of recast layer formation and worn-out analysis. *J. Mater. Res. Technol.* **2023**, *26*, 8569−8603.
(54) Wang, H.; Huang, Z.; Zeng, X.; Li, J.; Zhang, Y.; Hu, Q. Enhanced Anticarbonization and Electrical Performance of Epoxy Resin via Densified Spherical Boron Nitride Networks. *ACS Applied Electronic Materials* **2023**, *5* (7), 3726−3732.
(55) Channi, A. S.; Bains, H. S.; Grewal, J. S.; Chidambaranthan, V. S.; Kumar, R. Tool wear rate during electrical discharge machining for aluminium metal matrix composite prepared by squeeze casting: A prospect as a biomaterial. *J. Electrochem. Sci. Eng.* **2023**, *13* (1), 149−162.
(56) Sidhu, R. S.; Kumar, R.; Kumar, R.; Goel, P.; Singh, S.; Pimenov, D. Y.; Giasin, K.; Adamczuk, K. Joining of Dissimilar Al and Mg Metal Alloys by Friction Stir Welding. *Materials* **2022**, *15* (17), 5901.
(57) Kumar, R.; Singh, S.; Aggarwal, V.; Singh, S.; Pimenov, D. Y.; Giasin, K.; Nadolny, K. Hand and Abrasive Flow Polished Tungsten Carbide Die: Optimization of Surface Roughness, Polishing Time and Comparative Analysis in Wire Drawing. *Materials* **2022**, *15* (4), 1287.
(58) Kukureka, S. N.; Hooke, C. J.; Rao, M.; Liao, P.; Chen, Y. K. The effect of fibre reinforcement on the friction and wear of polyamide 66 under dry rolling−sliding contact. *Tribol Int.* **1999**, *32* (2), 107−116.
(59) Mishra, V.; Biswas, S. Three-body abrasive wear behavior of short jute fiber reinforced epoxy composites. *Polym. Compos.* **2016**, *37* (1), 270−278.
(60) Goyal, K. K.; Sharma, N.; Gupta, R. D.; Singh, G.; Rani, D.; Banga, H. K.; Kumar, R.; Pimenov, D. Y.; Giasin, K. A Soft Computing-Based Analysis of Cutting Rate and Recast Layer Thickness for AZ31 Alloy on WEDM Using RSM-MOPSO. *Materials* **2022**, *15* (2), 635.
(61) Kumar, R.; Bilga, P. S.; Singh, S. Multi objective optimization using different methods of assigning weights to energy consumption responses, surface roughness and material removal rate during rough turning operation. *Journal of Cleaner Production* **2017**, *164*, 45−57.
(62) Suresh, P. S.; Dilip Kumar, K.; Gautham, S. N.; Preetham, S.; Srinivasa, C. V.; Basavaraju, B. Tribological properties of areca sheath fiber composites. *Materials Today: Proceedings* **2021**, *46*, 7955−7961.
(63) Bhowmik, A.; Kumar, R.; Babbar, A.; Romanovski, V.; Roy, S.; Patnaik, L.; Kumar, J. P.; Alawadi, A. H. Analysis of physical, mechanical and tribological behavior of Al7075-fly ash composite for lightweight applications. *Int. J. Interactive Des. Manuf.* **2023**, 1−14.
(64) Sathyaseelan, P.; Sellamuthu, P.; Palanimuthu, L. Dynamic mechanical analysis of areca/kenaf fiber reinforced epoxy hybrid composites fabricated in different stacking sequences. *Materials Today: Proceedings* **2021**, *39*, 1202−1205.
(65) Jothibasu, S.; Mohanamurugan, S.; Vijay, R.; Lenin Singaravelu, D.; Vinod, A.; Sanjay, M. Investigation on the mechanical behavior of areca sheath fibers/jute fibers/glass fabrics reinforced hybrid composite for light weight applications. *Journal of Industrial Textiles* **2020**, *49* (8), 1036−1060.
(66) Bijwe, J.; Awtade, S.; Satapathy, B. K.; Ghosh, A. Influence of Concentration of Aramid Fabric on Abrasive Wear Performance of Polyethersulfone Composites. *Tribol. Lett.* **2004**, *17* (2), 187−194.
(67) Agarwal, G.; Patnaik, A.; Sharma, R. K. Parametric optimization and three-body abrasive wear behavior of sic filled chopped glass fiber reinforced epoxy composites. *Int. J. Compos. Mater.* **2013**, *3* (2), 32−38.
(68) Chand, N.; Naik, A.; Neogi, S. Three-body abrasive wear of short glass fibre polyester composite. *Wear* **2000**, *242* (1), 38−46.
(69) Siddhartha; Gupta, K. Mechanical and abrasive wear characterization of bidirectional and chopped E-glass fiber reinforced composite materials. *Materials & Design* **2012**, *35*, 467−479.
(70) Myshkin, N.; Pesetskii, S. S.; Grigoriev, A. Polymer Tribology: Current State and Applications. *Tribol. Ind.* **2015**, *37*, 284−290.
(71) Castano, F.; Cruz, Y. J.; Villalonga, A.; Haber, R. E. Data-driven insights on time-to-failure of electromechanical manufacturing devices: a procedure and case study. *IEEE Trans. Ind. Informatics* **2022**, 1−11.
(72) Yang, P.; Li, C.; Qiu, Y.; Huang, S.; Zhou, J., Metaheuristic Optimization of Random Forest for Predicting Punch Shear Strength of FRP-Reinforced Concrete Beams. *Materials* **2023**, *16* (11).
(73) Suenaga, D.; Takase, Y.; Abe, T.; Orita, G.; Ando, S. Prediction accuracy of Random Forest, XGBoost, LightGBM, and artificial neural network for shear resistance of post-installed anchors. *Structures* **2023**, *50*, 1252−1263.
(74) Badogu, K.; Thakur, V.; Kumar, R.; Kumar, R.; Singh, S., Acrylonitrile Butadiene Styrene-ZrO2 Composites for Roller Burnishing as Post-processing of 3D Printed Parts: Machine Learning Modeling Using Classification and Regression Trees. *Journal of Materials Engineering and Performance* **2023**.
(75) Ranjan, N.; Kumar, R.; Kumar, R.; Kaur, R.; Singh, S. Investigation of Fused Filament Fabrication-Based Manufacturing of ABS-Al Composite Structures: Prediction by Machine Learning and Optimization. *Journal of Materials Engineering and Performance* **2023**, *32* (10), 4555−4574.
(76) Pawanr, S.; Garg, G. K.; Routroy, S., Prediction of energy efficiency, power factor and associated carbon emissions of machine tools using soft computing techniques. *International Journal on Interactive Design and Manufacturing (IJIDeM)* 2022.
(77) Kiran, M. D.; B R, L. Y.; Babbar, A.; Kumar, R.; H S, S. C.; Shetty, R. P.; K B, S.; L, S. K.; Kaur, R.; Alkahtani, M. Q.; Islam, S.; Kumar, R. Tribological properties of CNT-filled epoxy-carbon fabric composites: Optimization and modelling by machine learning. *J. Mater. Res. Technol.* **2024**, *28*, 2582−2601.


https://doi.org/10.1021/acsomega.3c08164
*ACS Omega* 2024, 9, 8019−8036